https://doi.org/10.5194/egusphere-2025-1360
Preprint. Discussion started: 5 May 2025

Development of UI-WRF-Chem (v1.0) for the MAIA satellite mission: case demonstration

Huanxin Zhang[1,2], Jun Wang[1,2], Nathan Janechek[1,2], Cui Ge[1,2,‡], Meng Zhou[2,3,§], Lorena Castro García[1,2], Tong Sha[2], Yanyu Wang[2], Weizhi Deng[1,2], Zhixin Xue[1,2], Chengzhe Li[1,2], Lakhima Chutia[1,2], Yi Wang[2], Sebastian Val[4], James L. McDuffie[4], Sina Hasheminassab[4], Scott E. Gluck[4], David J. Diner[4], Peter R. Colarco[5], Arlindo M. da Silva[6]

[1]Department of Chemical and Biochemical Engineering, The University of Iowa, Iowa City, IA, 52242, United States
[2]Center for Global and Regional Environmental Research, The University of Iowa, Iowa City, IA, 52242, United States
[3]Interdisciplinary Graduate Program in Geo-Informatics, The University of Iowa, Iowa City, IA, 52242, United States
[4]NASA Jet Propulsion Laboratory, California Institute of Technology, Pasadena, CA, 91109, United States
[5]Atmospheric Chemistry and Dynamics Lab, NASA Goddard Space Flight Center, Greenbelt, MD, 20771, United States
[6]Global Modeling and Assimilation Office, NASA Goddard Space Flight Center, Greenbelt, MD, 20771, United States

[‡]Currently at: South Coast Air Quality Management District (AQMD), Diamond Bar, CA, 91765, United States
[§]Currently at: Goddard Earth Sciences Technology and Research (GESTAR) II, University of Maryland, Baltimore County, Baltimore, MD, 21250, United States

Correspondence to: Huanxin Zhang (huanxin-zhang@uiowa.edu), Jun Wang (jun-wang-1@uiowa.edu)

Abstract.

The Multi-Angle Imager for Aerosols (MAIA) satellite mission, to be jointly implemented by NASA and the Italian Space Agency with an expected 2026 launch, aims to study how different types of particulate matter (PM) pollution affect human health. The investigation will primarily focus on a discrete set of globally distributed Primary Target Areas (PTAs) containing major metropolitan cities, and will integrate satellite observations, ground observations, and chemical transport model (CTM) outputs to generate maps of near-surface total and speciated PM within the PTAs. In addition, the MAIA investigation will provide satellite measurements of aerosols over a set of Secondary Target Areas (STAs), which are useful for studying air quality more broadly. For the CTM, we have developed a Unified Inputs (of initial and boundary conditions) for WRF-Chem (UI-WRF-Chem) modeling framework to support the MAIA satellite mission. These developments include: (1) application of NASA GEOS FP and MERRA-2 data to provide both meteorological and chemical initial and boundary conditions for performing WRF-Chem simulations of air quality at a fine spatial resolution for both forecast and reanalysis modes; (2) a stand-alone emission preprocessor that ingests both global and regional anthropogenic emission inventories as well as fire emissions; (3) application of MODIS land data to improve land surface properties such as land cover type; (4) application of GLDAS and NLDAS data to constrain surface

https://doi.org/10.5194/egusphere-2025-1360
Preprint. Discussion started: 5 May 2025

soil properties such as soil moisture; (5) development of a new soil NO_x emission scheme – the Berkeley Dalhousie Iowa Soil NO Parameterization (BDISNP).

Here, we illustrate the model improvements because of these developments over four target areas: Beijing in China, CHN-Beijing (STA); Rome in Italy, ITA-Rome (PTA); Los Angeles in the U.S., USA-Angeles (PTA) and Atlanta in the U.S., USA-Atlanta (PTA). UI-WRF-Chem is configured as 2 nested domains using an outer domain (D1) and inner domain (D2) with a 12 km and 4 km spatial resolution, respectively. For each target area, we first run a suite of sensitivity simulations to test the model sensitivity to different options of physics schemes and then select the optimal combination of physics schemes based on evaluation of model simulated meteorology with ground observations. For the inner domain (D2), we have chosen to turn off the traditional Grell 3D ensemble (G3D) cumulus scheme. We conduct a case study over USA-Atlanta for June 2022 to demonstrate the impacts of cumulus scheme on precipitation and subsequent surface $PM_{2.5}$ concentration. Our results show that keeping the G3D cumulus scheme on results in higher precipitation and lower $PM_{2.5}$ than the simulation with the G3D cumulus scheme off. Compared with surface observations of precipitation and $PM_{2.5}$ concentration, the sensitivity simulation with the G3D scheme off shows better performance than keeping it on. We focus on two dust intrusion events over CHN-Beijing and ITA-Rome, which occurred in March 2018 and June 2023, respectively. We carry out a suite of sensitivity simulations using UI-WRF-Chem by excluding chemical boundary conditions or including MERRA-2 chemical boundary conditions. Our results show that using MERRA-2 data to provide chemical boundary conditions can help improve model simulation of surface PM concentration and AOD. Some of the target areas have also experienced significant changes in land cover and land use over the past decade. Our case study over CHN-Beijing in July 2018 investigates the impacts of improved land surface properties with timely MODIS land data on capturing the urban heat island phenomenon. Model-simulated surface skin temperature shows better agreement with MODIS observed land surface temperature. The updated soil NO_x emission scheme in July 2018 also leads to higher NO_2 vertical column density (VCD) in rural areas over CHN-Beijing target area, which matches better with TROPOMI observed NO_2 VCD. This in turn affects the simulation of surface nitrate concentration. Lastly, we conduct a case study over USA-LosAngeles to tune the dust emissions. This gives an example to show the fine-tuning work we do over each target area to investigate the problem specific to that target area as we continue evaluating and improving model performance.

1. Introduction

Ambient particulate matter (PM) pollution has been ranked as one of top environmental risk factors for global deaths (Forouzanfar et al., 2016). The integrated use of satellite and chemical transport model (CTM) outputs have shed light on the impacts of $PM_{2.5}$ (PM with aerodynamic diameter less than 2.5μm) on public health in the past decade (Cohen et al., 2017; Wang et al., 2021a). Satellite retrieved aerosol data products such as aerosol optical depth (AOD) have been widely

https://doi.org/10.5194/egusphere-2025-1360
Preprint. Discussion started: 5 May 2025

used to estimate ground-level $PM_{2.5}$ concentration over the past two decades (e.g. (Shin et al., 2020; Van Donkelaar et al., 2006; Wang and Christopher, 2003)) due to its large spatial coverage. Because of the uncertainty in remote sensing technique and the complex AOD-$PM_{2.5}$ relationship (Wang and Christopher, 2003), these satellite derived ground-level $PM_{2.5}$ have been combined with ground observations of $PM_{2.5}$ and/or CTM simulated $PM_{2.5}$ to form a hybrid method of providing a new data source for epidemiological health studies (e.g. (Van Donkelaar et al., 2010; Holloway et al., 2021; Diao et al., 2019)). This hybrid method has also been used for estimating $PM_{2.5}$ component concentration and its application in health-related studies (Philip et al., 2014; Li et al., 2021; Hu et al., 2019; Wei et al., 2023).

The Multi-Angle Imager for Aerosols (MAIA) satellite mission to be jointly implemented by the National Aeronautics and Space Administration (NASA) (Diner et al., 2018) and the Italian Space Agency (ASI) has a key objective to map the PM composition and study the impacts of different types of PM on human health (Liu and Diner, 2017). The MAIA instrument builds upon the work of the Multi-angle Imaging SpectroRadiometer (MISR) instrument, onboard NASA's Terra spacecraft, which has been retrieving aerosol properties including aerosol type since February 2000 (Diner et al., 1998; Kahn et al., 2005). MISR has also been one of the commonly used satellite instruments for mapping global PM concentration for studying air quality and public health (Liu et al., 2009; Holloway et al., 2021; Meng et al., 2018). The MAIA investigation will focus on a set of primary target areas (PTAs) globally (https://maia.jpl.nasa.gov/mission/#target_areas), which are large metropolitan areas. For each PTA, it will integrate satellite observations, CTM outputs and ground observations to generate maps of surface total and speciated PM including sulfate, nitrate, dust, Organic Carbon (OC) and Black Carbon (BC) or Elemental Carbon (EC). In addition, the MAIA investigation will provide satellite measurements of aerosols over a set of Secondary Target Areas (STAs), which are useful for studying air quality more broadly.

Our work here introduces the development of the Unified Inputs (of initial and boundary conditions) for WRF-Chem (UI-WRF-Chem) as the CTM for supporting the MAIA satellite mission, based on the standard WRF-Chem model (Fast et al., 2006; Grell et al., 2005). The major updates we have made include the following: (1) application of the NASA Goddard Earth Observing System (GEOS) products including both GEOS Forward Processing (FP) and Modern-Era Retrospective Analysis for Research and Application, version 2 (MERRA-2) data to provide both meteorological and chemical initial and boundary conditions for performing WRF-Chem simulation with a finer spatial resolution in forecasting and reanalysis modes; (2) development of a stand-alone WRF-Chem Emission Preprocessing System (WEPS) that ingests both global and regional anthropogenic emission inventories as well as fire emissions; (3) application of Moderate Resolution Imaging Spectroradiometer (MODIS) land data to update land surface properties such as land cover type in WRF-Chem; (4) application of the Global Land Data Assimilation System (GLDAS) (Rodell et al., 2004) or the North American Land Data Assimilation System (NLDAS) (Mitchell et al., 2004) data to constrain soil properties such as soil moisture; and (5) development of a new soil NO_x ($NO + NO_2$) emission scheme - the Berkeley Dalhousie Iowa Soil NO

https://doi.org/10.5194/egusphere-2025-1360
Preprint. Discussion started: 5 May 2025

Parameterization (BDISNP), based on the Berkeley Dalhousie Soil NO Parameterization (BDSNP) (Hudman et al., 2012).

The new developments of UI-WRF-Chem are justified with the following consideration. First, the NASA GEOS system assimilates satellite observations of aerosol products (Randles et al., 2017). Using these assimilated data to provide chemical initial and boundary conditions for WRF-Chem simulations over MAIA target areas would be computationally efficient for capturing long-range or regional transport without enlarging the model domain to include the emission sources. A number of studies have demonstrated the influence of chemical boundary conditions on regional air pollution in the domain of interests when running WRF-Chem (e.g. (Mo et al., 2021; Ukhov et al., 2020; Roozitalab et al., 2021; Wang et al., 2004)). Second, anthropogenic and fire emissions play a crucial role in simulating aerosols in the CTM. Building our own emission preprocessor will allow us the opportunities to optimize the existing emission inventories and add new ones, especially those from top-down estimates (Wang et al., 2020b; Wang et al., 2020c). Third, some of the default land surface properties used in WRF-Chem such as land cover type have been out of date. Using MODIS land data to update land surface properties in a timely manner would help improve mesoscale model performances (Li et al., 2014; Li et al., 2017a; Aegerter et al., 2017; Wang et al., 2023). Fourth, soil properties such as soil moisture fields are of the high importance to both weather forecast, biogenic emission estimates and dust storm simulation (Han et al., 2021), and ultimately, air quality prediction (Thomas et al., 2019; Jenkins and Diokhane, 2017; De Rosnay et al., 2014). The GLDAS and NLDAS are two data assimilation systems that can offer optimized initial soil conditions with a high spatial and temporal resolution for numerical weather forecasting (Dillon et al., 2016; Xia et al., 2014). Better estimates of soil moisture will also lead to improved simulation of soil NO_x emissions, which serve as an important part of the total global NO_x budget (Jaeglé et al., 2005) and also play a critical role in the formation of ozone (O_3) and nitrate aerosols (Sha et al., 2021; Lin et al., 2021). Lastly, the default soil NO_x emissions in WRF-Chem could be underestimated by a factor of 10 in some places (Oikawa et al., 2015).

In this paper, we present the developments of the UI-WRF-Chem modeling framework and then illustrate the model improvement as the results of some of these developments as well as fine tuning over a specific target area. In this work, we focus on four target areas: Three of the target areas are PTAs: Rome in Italy (ITA-Rome), Los Angeles in the U.S. (USA-LosAngeles) and Atlanta in the U.S. (USA-Atlanta); one is a STA: Beijing in China (CHN-Beijing). Beijing was a PTA and has recently been changed to a STA. However, the case study over Beijing can still serve as a good example to demonstrate the model capability. These four target areas together have a good representation of the range of PM pollution levels across the target areas (Los Angeles and Atlanta on the lower end, Rome in the middle and Beijing on the higher end). Some of our previous work have focused on other PTAs using the UI-WRF-Chem modeling framework. Li et al. (2024) developed an inverse modeling method to improve the diurnal profile of anthropogenic emissions in Addis Ababa, Ethiopia PTA, using surface observations from both U.S. Embassy sites and PurpleAir sensors. Chutia et al. (2024) investigated the impacts of aerosol-radiation interaction on

https://doi.org/10.5194/egusphere-2025-1360
Preprint. Discussion started: 5 May 2025

air quality in Delhi, India PTA. Overall, current work together with previous work can provide a good picture of the model performance for different applications. This paper is organized as follows: Section 2 focuses on the description of the UI-WRF-Chem model development; Section 3 provides the model configuration used in the target areas; Results and Conclusion are presented in Section 4 and Section 5, respectively.

2. UI-WRF-Chem development

UI-WRF-Chem uses the NASA GEOS model data to provide self-consistent and unified meteorological and chemical initial and boundary conditions for driving WRF-Chem simulations. UI-WRF-Chem can be run in both forecasting and reanalysis modes, which are driven by GEOS FP and MERRA-2 meteorology and aerosol fields, respectively. Both modes are needed because the former is used in MAIA's near real time (NRT) data production, while the latter is used in MAIA's reanalysis postprocessing data production.

2.1 Unified Inputs (of initial and boundary conditions) for meteorology and chemistry

Both GEOS FP and MERRA-2 data are generated within the GEOS atmospheric and data assimilation system (Rienecker et al., 2008), in which meteorological and aerosol observations are jointly assimilated. GEOS FP uses the most recent GEOS system to produce the real-time forecasting data while MERRA-2 uses a frozen version of the GEOS system to conduct the long-term atmospheric reanalysis since 1980. The GEOS native model is on a cubed sphere grid with 72 hybrid-eta layers from surface to 0.01 hPa. Products are saved on a 0.5º x 0.625º latitude by longitude grid for MERRA-2 and 0.25º x 0.3125º latitude by longitude for GEOS FP (Gelaro et al., 2017).

MERRA-2 assimilates multiple streams of aerosol products including bias corrected AOD calculated from observed radiances measured by the Advanced Very High Resolution Radiometer (AVHRR) over ocean prior to 2002 and by MODIS on Terra and Aqua satellites over dark surfaces and ocean since 2000 and 2002, respectively; also assimilated are the MISR AOD over bright land surface and AOD measurements from Aerosol Robotic Network (AERONET) before 2014 (Randles et al., 2017). In the NRT mode, GEOS FP only assimilates AOD derived from MODIS Terra and Aqua. The aerosol module used in the GEOS system is the Goddard Chemistry, Aerosol, Radiation, and Transport (GOCART) model (Colarco et al., 2010; Chin et al., 2002). The GOCART module simulates major aerosol species including sulfate, BC, OC, dust (five bins with lower and upper radius range as: 0.1–1, 1–1.8, 1.8–3, 3–6, 6–10 μm), and sea salt (five bins with lower and upper radius range as: 0.03–0.1, 0.1–0.5, 0.5–1.5, 1.5–5.0, 5.0–10 μm). These aerosol products are available in both GEOS FP and MERRA-2 products. Since 2017, nitrate aerosols have been added into the GEOS system and GEOS FP products thus include nitrate aerosols.

https://doi.org/10.5194/egusphere-2025-1360
Preprint. Discussion started: 5 May 2025

Our work differs from the past work that uses the GEOS FP or MERRA-2 data to drive WRF-Chem in several aspects. For example, Peters-Lidard et al. (2015) presented the NASA Unified-Weather Research and Forecasting model (NU-WRF) that can be driven by GEOS FP and MERRA-2, but its atmospheric chemistry process is simplified with the GOCART module (without prognostic simulation of aerosol size distribution and nitrate for example) and is designed to be an observation driven integrated modeling system that represents aerosol, cloud, precipitation, and land processes at satellite-resolved scales (~1–25 km). Hence, its real-time application for atmospheric chemistry and aerosol composition forecast is rather limited. Nevertheless, the NU-WRF's concept and framework of using GEOS FP and MERRA-2 to drive WRF-Chem are adopted by UI-WRF-Chem development here to provide meteorological initial and boundary conditions for WRF-Chem, using meteorological variables other than soil properties.

Adopting of GEOS FP or MERRA-2 soil properties into WRF-Chem needs special treatment. In the GEOS system, the land surface model (LSM) is a catchment-based model (Koster et al., 2000), which is fundamentally different from the LSMs available in WRF-Chem. The commonly used LSMs in WRF-Chem include the Noah scheme (Chen et al., 1996; Chen and Dudhia, 2001), the Rapid Update Cycle (RUC) (Smirnova et al., 2000), and the Community Land Model (CLM) (Oleson et al., 2004), which are all column-based models with different soil layers. To resolve this issue, Peters-Lidard et al. (2015) used the Land Information System (LIS) (Kumar et al., 2006) to process GEOS outputs and provide initial conditions of soil properties such as soil temperature and soil moisture for running WRF and NU-WRF (Kumar et al., 2008). Since land surface process is slow and usually requires years of LIS simulation to stabilize the soil properties in the model, we have here developed modules to utilize soil data products from two land data assimilation systems, GLDAS (Rodell et al., 2004) and NLDAS (Mitchell et al., 2004), which use LIS to focus on the analysis of soil properties in near real time. This way, we reduce the computational cost and complexity of running LIS within the UI-WRF-Chem. The initial conditions of soil properties can have an important impact on boundary layer processes for days to weeks (the so-called memory effect). Hence, the special treatment of soil properties by using observation-constrained GLDAS and NLDAS in UI-WRF-Chem is warranted.

Our use of GEOS FP and MERRA-2 as UI-WRF-Chem chemical boundary conditions also differs from the common practice that is adopted by either Community Atmosphere Model with Chemistry, CAM-Chem (Emmons et al., 2020) for reanalysis or the Whole Atmosphere Community Climate Model (WACCM) (Gettelman et al., 2019) for NRT forecasts as WRF-Chem's chemical boundary conditions. Both CAM-Chem and WACCM don't assimilate satellite-based aerosol fields and therefore lack the observational constraints for the day-to-day change of aerosols concentration for a domain of interest.

Finally, we have also developed a method to constrain the chemical boundary condition for the allocation of dust concentration in the MERRA-2 data as a function of different dust size bins. This method can be applied in areas where AERONET sites with long-term data are available. We

https://doi.org/10.5194/egusphere-2025-1360
Preprint. Discussion started: 5 May 2025

compare the dust particle size distribution (PSD) from MERRA-2 data with AERONET observations to better distribute the dust concentration into different size bins in the chemical boundary conditions. Detailed description and application of this approach are described in Sect 4.1 and 4.2.

2.2 Updates of land surface properties and soil NO_x emission scheme

We also develop capabilities within UI-WRF-Chem to update land surface properties in a timely manner. In the current work, we have selected the Noah LSM as the land surface model. MODIS land products are used to update the land surface properties including land cover type on the annual basis, green vegetation fraction (GVF), leaf area index (LAI) and surface albedo on the monthly basis in the Noah LSM. These variables are among the key surface properties in the land model that regulate the exchanges of energy, water, and momentum (Mölders, 2001). The major technical development and its application to study the impacts of land use/cover changes on urban temperature in Eastern China during 2003–2019 were described in Wang et al. (2023). Below we briefly describe the updates of each land surface property.

The WRF-Chem model provides different sources of data for land surface properties. For land cover type, one is the U.S. Geological Survey (USGS) map with 24 land cover types, which is derived from the monthly AVHRR Normalized Difference Vegetation Index (NDVI) observations from April 1992 to March 1993. Another one is from the MODIS land cover data including 17 land cover types, based on the International Geosphere-Biosphere Program (IGBP) scheme (Friedl et al., 2002) and three classes of tundra (Justice et al., 2002). Over the years, MODIS land cover data used in the WRF-Chem community have been updated for year 2001, 2004 or climatology data from 2001–2010 (Broxton et al., 2014). For GVF, the default one was derived based on the AVHRR NDVI observations collected from 1985 to 1990. Another option is to use the MODIS Fraction of Absorbed Photosynthetically Active Radiation (FPAR) (data are from the early 2000s) to substitute for GVF. For LAI and surface albedo, one option is to calculate the values online using the look-up table, based on each land cover type. Another option is to use the MODIS LAI and albedo data directly (data provided are from the early 2000s).

Here, we have developed the capability to update all the four land surface properties in UI-WRF-Chem via the WRF Preprocessing System (WPS) in a timely fashion. It provides self-consistence among the key land surface properties used in the land model as they come from the same satellite observations and offers a flexible way to apply the data for WRF-Chem simulations with different spatial resolution. The land cover data are updated with the MODIS yearly land cover type product (MCD12Q1) collection 6 with a spatial resolution of 500 m. The LSM scheme also allows the alternative use of satellite datasets for updating LAI, GVF and surface albedo. We develop two ways to update GVF in the model: (1) using the recent MODIS NDVI product (MOD13A3) to derive GVF; (2) using the Fraction of Photosynthetically Active Radiation absorbed by vegetation (FPAR) from MODIS MCD15A2H product to replace GVF. For LAI, we use the MODIS LAI

https://doi.org/10.5194/egusphere-2025-1360
Preprint. Discussion started: 5 May 2025

product (MCD15A2H) to update it in the model. For surface albedo, we have the option to use two MODIS data products to update it in the model: (1) using the MCD43A3 albedo products; (2) using the MODIS combined Terra and Aqua Bidirectional Reflectance Distribution Function (BRDF) and Albedo product (MCD43C3).

The new BDISNP soil NO_x emission scheme is also integrated as part of the UI-WRF-Chem framework. The detailed development of the scheme has been described in Sha et al. (2021) and Wang et al. (2021c). Briefly, in the standard WRF-Chem model, soil NO_x emissions are calculated using the Model of Emissions of Gases and Aerosols from Nature (MEGAN) (Guenther et al., 2006; Guenther et al., 2012), which is intended for estimating biogenic emissions of volatile organic compounds (VOCs). In the MEGAN model, emission factors are based on four global plant function types (broadleaf trees, needle-leaf trees, shrubs/bushes and herbs/crops/grasses). Previous work by Oikawa et al. (2015) has suggested that soil NO_x emissions calculated from the MEGAN model using WRF-Chem can be a factor of 10 underestimated in the Imperial Valley, California, compared with ground observations. The BDSNP soil NO_x emission scheme, currently implemented in the global 3-D GEOS-Chem model (Hudman et al., 2012), was added into the UI-WRF-Chem, as the BDISNP, with several of our own updates.

As in BDSNP, the BDISNP includes a more physical representation of the soil NO_x emission process compared with the MEGAN model. The BDISNP considers available nitrogen (N) in soils from biome specific emission factors, online dry and wet deposition of N, and fertilizer and manure N. It also includes the pulsing of soil NO_x emission following soil wetting by rain and the impacts of soil temperature and moisture. Compared to BDSNP, we have made four major updates in the BDISNP: (1) updating the land cover type data with the MODIS land cover type data to better reflect the land cover change; (2) using the GLDAS soil temperature data for calculating the soil NO_x emissions rather than using the 2 m air temperature as a proxy for soil temperature; (3) using the modelled GVF data to determine the distribution of arid and non-arid regions to replace the static climate data used in the BDSNP scheme. With these three updates, Sha et al. (2021) has shown that the WRF-Chem simulation with the BDISNP scheme leads to a better agreement with TROPOMI retrieved NO_2 columns over California for July 2018, compared with using the default MEGAN scheme. The increased soil NO_x emissions with the BDISNP scheme result in a 34.7% increase in monthly mean NO_2 columns and 176.5% increase in surface NO_2 concentration, which causes an additional 23.0% increase in surface O_3 concentration in California. The work of Zhu et al. (2023) used derived soil NO_x flux measurements from a field Campaign over the San Joaquin Valley in California during June 2021 to evaluate three soil NO_x emission schemes: the MEGAN in the California Air Resource Board (CARB) emission inventory, the Biogenic Emission Inventory System (BEIS) and the BDISNP developed here. It was found that both MEGAN and BEIS inventories were lower than the observation by more than one order of magnitude, and the BDISNP was lower by a factor of 2.2. Even though being underestimated, the BDISNP and the observation showed a similar spatial pattern and temperature dependence.

https://doi.org/10.5194/egusphere-2025-1360
Preprint. Discussion started: 5 May 2025

The fourth update revises the default soil temperature response function in the BDISNP scheme, as described in Wang et al. (2021c). In the default scheme, the soil temperature response follows an exponential function for soil temperature between 0 °C and 30 °C and stays the same as 30 °C after the soil temperature is above 30 °C. In the work of Oikawa et al. (2015), which found high soil NO_x emissions in high-temperature agricultural soils, an observation-based soil temperature response function was developed. This function is used here to update the default soil temperature response function. Specifically, in the range of 20 °C and 40 °C, it is a cubic function of soil temperature. When soil temperature is greater than 40 °C, the value of the response function is set the same as the value of soil temperature at 40 °C. In addition, final soil NO_x emissions are reduced by 50% following the work of Silvern et al. (2019) and Vinken et al. (2014). With this update, Wang et al. (2021c) showed that the GEOS-Chem simulated tropospheric NO_2 vertical column densities (VCDs) agrees better with Ozone Monitoring Instrument (OMI) observed NO_2 VCDs for 2005–2019 summer in the U.S., compared with the GEOS-Chem simulation that uses the default soil temperature function. This model improvement further helps explain the slowdown of tropospheric NO_2 VCD reduction during 2009–2019 observed by OMI in the U.S.

2.3 WRF-Chem Emission Preprocessing System (WEPS)

The WEPS Fortran utility is developed to map both global and regional anthropogenic emissions as well as fire emissions for running UI-WRF-Chem simulations. WEPS builds upon a few tools used in the WRF-Chem community (https://www2.acom.ucar.edu/wrf-chem/wrf-chem-tools-community). For example, the anthro-emiss utility creates WRF-Chem ready emission files from global anthropogenic emission inventory datasets. There is also another Fortran program (emission_v3.F) to process the U.S. EPA National Emissions Inventory (NEI) 2005 and 2011. Recently, a new tool EPA_ANTHRO_EMIS has been developed to create WRF-Chem ready anthropogenic emission files from Sparse Matrix Operator Kernel Emissions (SMOKE) Modeling System netcdf outputs for NEI 2014 and 2017. We have adopted some of the functionalities in these tools into the WEPS.

Currently in WEPS, we can ingest the following global anthropogenic emission inventories: (1) HTAP_v2.2 (Janssens-Maenhout et al., 2015) and HTAP_v3 (Crippa et al., 2023), created under the umbrella of the Task Force on Hemispheric Transport of Air Pollution (TF HTAP), which is the compilation of different emission inventories over specific regions (North America, Europe, Asia including Japan and South Korea) with the independent Emissions Database for Global Atmospheric Research (EDGAR) inventory filling in for the rest of the world; (2) EDGARv5.0 for year 2015 (Crippa et al., 2020). The HTAP_v3 includes regional emission inventories from U.S. EPA NEI, CAMS-REGv5.1 for Europe, the Regional Emission inventory in Asia (REASv3.2.1), the Clean Air Policy Support System (CAPSS-KU) inventory over South Korea, the JAPAN emission inventory (PM2.5EI and J-STREAM) in Japan and EDGARv6.1 (https://data.jrc.ec.europa.eu/dataset/df521e05-6a3b-461c-965a-b703fb62313e) for the rest of the

https://doi.org/10.5194/egusphere-2025-1360
Preprint. Discussion started: 5 May 2025

world. It consists of 0.1 ° x 0.1 ° grid maps of species: CO, SO_2, NO_x, non-methane volatile organic compound (NMVOC), NH_3, PM_{10}, $PM_{2.5}$, BC and OC for year 2000–2018 (Crippa et al., 2023). Four sectors are included for these species: energy (mainly power industry), industry (manufacturing, mining, metal, cement, etc.), transport (ground transport such as road) and residential (heating/cooling of buildings etc.). For NH_3, an additional sector – agriculture is also included. The datasets have a monthly temporal resolution, and we have interpolated them to daily data. In addition, we have added sector-based diurnal profiles following the work of Du et al. (2020). For UI-WRF-Chem simulation over the U.S. domain or China domain, we have added the capability to use U.S. EPA NEI 2017 or the Multi-resolution Emission Inventory model for Climate and air pollution research (MEIC) (Zheng et al., 2018; Li et al., 2017b) emission inventory to replace the global emission inventory HTAP_v3, respectively.

For fire emissions, the WEPS can process several emission inventories as described in Zhang et al. (2014). They include: Fire Locating and Modeling of Burning Emissions inventory (FLAMBE) (Reid et al., 2009); Fire INventory from NCAR version 1.0 (FINN v1.01) (Wiedinmyer et al., 2011); Global Fire Emission Database version 3.1 (GFED v3.1) (Van Der Werf et al., 2010); Fire Energetics and Emissions Research version 1.0 using fire radiative power (FRP) measurements from the geostationary Meteosat Spinning Enhanced Visible and Infrared Imager (FEER-SEVIRI v1.0) (Roberts and Wooster, 2008; Ichoku and Ellison, 2014); Global Fire Assimilation System (GFAS v1.0) (Kaiser et al., 2012); NESDIS Global Biomass Burning Emissions Product (GBBEP-Geo) (Zhang et al., 2012); Quick Fire Emissions Dataset version 2.4 (QFED v2.4) (Darmenov and Da Silva, 2015). Our recent work involves developing a Visible Infrared Imaging Radiometer Suite (VIIRS) based fire emission inventory, FIre Light Detection Algorithm (FILDA-2) (Zhou et al., 2023). Our past work has mainly focused on OC and BC emissions from FLAMBE emission inventory (e.g. (Ge et al., 2014; Zhang et al., 2022; Zhang et al., 2020)). We have now included gas species such as CO from FLAMBE emission inventory. The injection height by default is set to range from 500 m to 1200 m, based on our previous work (e.g. (Yang et al., 2013; Wang et al., 2013; Ge et al., 2017)) and users have the option to specify the injection height on their own.

2.4 WRF-Chem chemistry description and update

The MAIA investigation not only focuses on the total $PM_{2.5}$ and PM_{10} mass but the speciated $PM_{2.5}$ including sulfate, nitrate, BC or EC, OC and dust. We have therefore selected the Regional Acid Deposition Model, Version 2 (RADM2) for gas-phase chemistry (Stockwell et al., 1990) and the Modal Aerosol Dynamics model for Europe (MADE) (Ackermann et al., 1998) and the Secondary ORGanic Aerosol Model (SORGAM) (Schell et al., 2001) as the aerosol module for MAIA model simulations, using WRF-Chem Version v3.8.1. The RADM2-MADE/SORGAM chemistry mechanism in WRF-Chem simulates the above-mentioned aerosol species and has been widely used to study air quality (e.g. (Georgiou et al., 2018; Zhang et al., 2020; Tuccella et al., 2012)). The MADE/SORGAM aerosol module also includes ammonium, sea salt and water. The aerosol

https://doi.org/10.5194/egusphere-2025-1360
Preprint. Discussion started: 5 May 2025

size distribution is represented by the modal approach (Binkowski and Shankar, 1995), which uses three modes (the Aitken, accumulation and coarse mode). A log-normal size distribution and internal mixing of aerosol species are assumed in each mode.

In the MADE/SORGAM aerosol scheme, dust is not explicitly simulated but rather blended into other species. For smaller size bins of dust, they are represented by the unspecified $PM_{2.5}$ chemical species, which have Aitken and accumulation modes. For larger size bins of dust, they are counted as the "soila", which are used for coarse soil-derived aerosol species. To output the dust proportion of the surface $PM_{2.5}$ mass concentration, we add dust species in five size bins (same as the GOCART dust bins in MERRA-2) into the MADE/SORGAM aerosol scheme. This way, when using MERRA-2 or GEOS FP to provide chemical initial and boundary conditions, the dust species from the boundary file can be consistent with the dust species in the aerosol scheme. WRF-Chem currently provides three dust emission schemes: the original GOCART dust emission scheme (Ginoux et al., 2001), GOCART dust emission with the Air Force Weather Agency (AFWA) modifications (Legrand et al., 2019), and the University of Cologne (UOC) scheme (Shao et al., 2011). Both GOCART and GOCART-AFWA emission schemes release dust in five size bins with lower and upper radius range of 0.1–1, 1–1.8, 1.8–3, 3–6, 6–10 μm, same as the dust size bin used in the MERRA-2 system. The UOC dust emission scheme considers dust in four size bins with lower and upper radius range of 0–1.25, 1.25–2.5, 2.5–5, and 5–10 μm. Here, we have selected the use of GOCART-AFWA emission scheme in the UI-WRF-Chem framework, which matches the dust size bins in the MERRA-2 and GEOS FP aerosol scheme.

Subsequently, a new chemistry scheme (MADE/SORGAM-DustSS) is created in UI-WRF-Chem to include the dust in five size bins and sea salt aerosols as additional chemical tracers while all other gas and aerosol species are the same as in the MADE/SORGAM scheme. The standard WRF-Chem model currently supports the GOCART sea salt emission scheme, which releases sea salt aerosol species in four bins. The lower and upper radius range of sea salt aerosols species are: 0.1–0.5, 0.5–1.5, 1.5–5.0, 5.0–10 μm. We have then added sea salt aerosols in these four bins into the MADE/SORGAM-DustSS scheme in the UI-WRF-Chem framework. The GOCART sea salt aerosols in MERRA-2 data have five bins with lower and upper radius range as: 0.03–0.1, 0.1–0.5, 0.5–1.5, 1.5–5.0, 5.0–10 μm. This way, the GOCART sea salt aerosols in the aerosol scheme would also match the aerosols in the chemical boundary file provided by MERRA-2 data. In the newly added scheme of MADE/SORGARM-DustSS, we have followed the simple GOCART aerosol scheme in the standard WRF-Chem model to add different transport processes for dust and sea salt aerosol species such as dry deposition. We have also added a simple wet scavenging scheme for dust and sea seal aerosols, which is described more in Sect 4.2.

Aerosol optical properties such as extinction and single scattering albedo are calculated based on a sectional approach (Barnard et al., 2010) with 8 bins in WRF-Chem, regardless of the aerosol scheme selected. For aerosol species in the MADE/SORGAM-DustSS aerosol scheme, the mass and number concentrations of each aerosol species in the three modes will be matched to the 8

https://doi.org/10.5194/egusphere-2025-1360
Preprint. Discussion started: 5 May 2025

bins. For dust and sea salt aerosol species, the dust and sea salt aerosols in their original 5 and 4 bins, are matched to the 8 bins. In each bin, the particles are assumed to be internally mixed and spherical. The bulk properties such as refractive index for each bin is based on volume approximation. Then, Mie theory is called to calculate the optical properties such as the absorption efficiency and asymmetry parameter for each bin. The optical properties are computed and outputted at four wavelengths (300, 400, 600 and 1000 nm). In addition, the work of Ukhov et al. (2021) has found a few inconsistencies in WRF-Chem related to dust emissions coupled with the GOCART aerosol module, which also impacts other aerosols schemes such as the MADE/SORGAM module. These inconsistencies were found in the calculation of surface $PM_{2.5}$ and PM_{10} concentration, calculation of aerosol optical properties and estimation of gravitational settling. We have incorporated the corrections of these inconsistencies made by Ukhov et al. (2021) in our UI-WRF-Chem framework.

2.5 Postprocessing and evaluation code, and repository management

Python modules are developed in house to postprocess UI-WRF-Chem hourly outputs as part of the UI-WRF-Chem framework. They include diagnostics of some commonly used variables which are not directly outputted such as relative humanity (RH) and the capability to extract and compile hourly model output into daily output to facilitate file management. We have also created python modules to evaluate UI-WRF-Chem model performance against ground observations and satellite data, e.g., comparing model simulated column concentration of trace gases NO_2 with satellite observed column concentration of NO_2. In addition, bash scripts are developed to automatically run UI-WRF-Chem framework for both forecasting and reanalysis modes. It needs minimal work to specify the paths of the codes and data on the servers before running the UI-WRF-Chem model. The UI-WRF-Chem framework uses the GitHub, a git-based version control system to manage its codes and developments. The repository stores the main codes of UI-WRF-Chem. When major developments from our group and collaborators are made and validated, a new version will be released. The WRF-Chem community also updates the WRF-Chem code and releases new versions periodically, we will also check the major bug fixes and developments to incorporate them in our codes accordingly.

3. Model configuration

All the UI-WRF-Chem model simulations for MAIA target areas are set up as 2 nested domains (Fig 1) with a 4 km x 4 km horizontal spatial resolution for the inner domain (D2) focusing on the MAIA target area and a 12 km x 12 km horizontal spatial resolution for a larger outer domain (D1). The inner and outer domain have nominal dimension of ~360 km (east-west) x 480 km (north-south) and ~1080 km (east-west) x 1000 km (north-south), respectively. Both domains have 48 vertical levels extending from the surface to 50 hPa. For the inner domain (D2), we have turned off the cumulus scheme to let the model fully resolve the convective process while all other model configurations are the same for both domains.

https://doi.org/10.5194/egusphere-2025-1360
Preprint. Discussion started: 5 May 2025

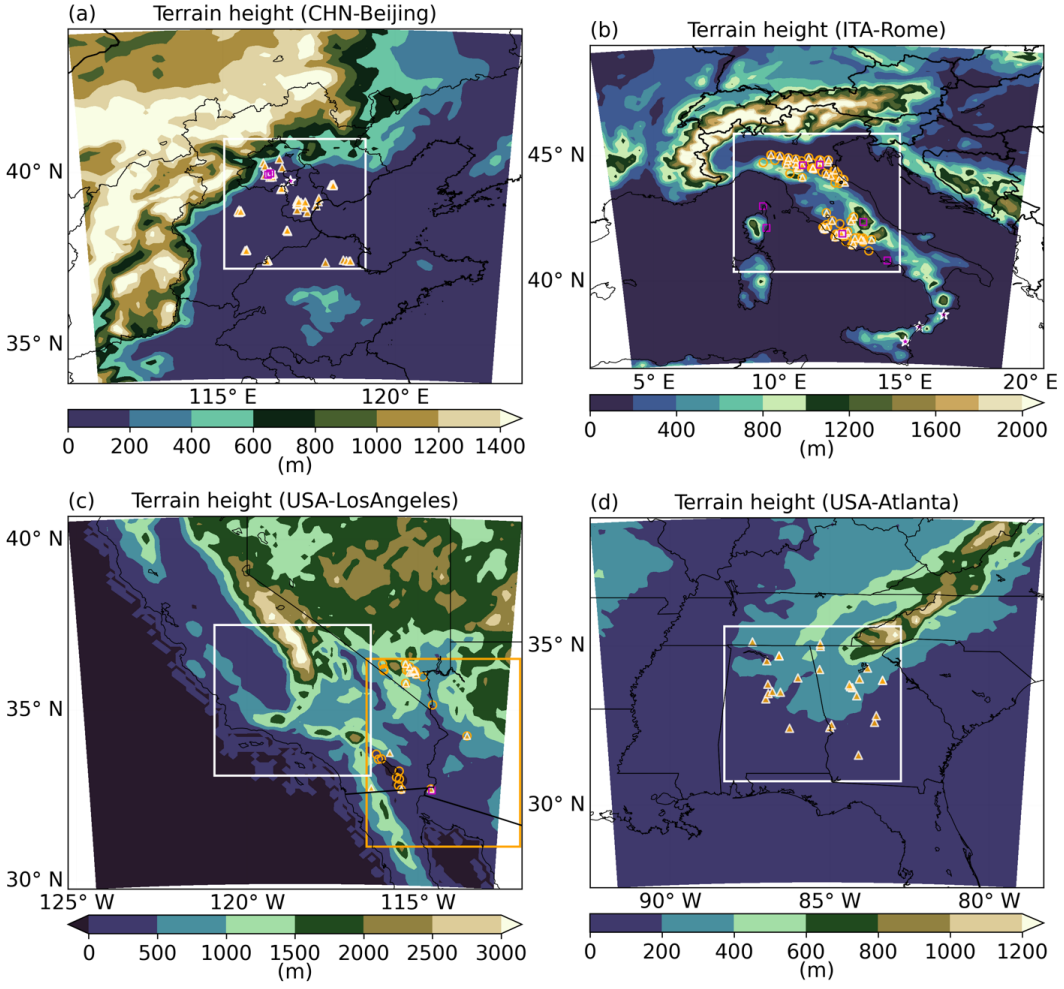

Figure 1. Terrain height for (a) CHN-Beijing, (b) ITA-Rome, (c) USA-LosAngeles and (d) USA-Atlanta target areas of the 2 nested domains: the outer domain (D1) and the inner domain (D2) shown as the white box. For (a), the orange filled triangles represent the ground observation sites of $PM_{2.5}$ and PM_{10} mass concentration. Both open magenta squares and stars represent the AERONET ground observation sites. The sites denoted by the stars are used to constrain the dust particle size distribution as described in Sect 4.1 while the sites denoted by squares are used to evaluate model simulated AOD. (b) is same as (a), except that the orange open circles represent ground observations of PM_{10} mass concentration, and orange filled triangles are the ground observations sites of $PM_{2.5}$ mass concentration. (c) is the same as (b) except that the orange box is defined as the dust-prone region, which is used to tune dust emissions. For (d), the orange filled triangles represent the ground observation sites of $PM_{2.5}$ mass concentration.

For each target area, we first run a suite of sensitivity simulations to test the model sensitivity to different options of the physics schemes by evaluating model simulated meteorology variables

https://doi.org/10.5194/egusphere-2025-1360
Preprint. Discussion started: 5 May 2025

with ground observations and then select the optimal combination of physics schemes based on evaluation results. A description of the satellite and ground observation datasets used are provided in Text S1 of the supporting information (SI). Several statistics are used to evaluate the model performance against ground and satellite observations, including linear correlation coefficient (*R*), root mean square error (RMSE), mean bias (MB), normalized mean bias (NMB), normalized standard deviation (NSD) and normalized centered root mean square error (NCRMSE). NSD is the ratio of the standard deviation of the model simulation to the standard deviation of the observation. NCRMSE is like RMSE except that the impact of the bias is removed. Some of the aforementioned statistics are summarized in a Taylor Diagram (Taylor, 2001), which includes *R* (shown as the cosine of the polar angle), NSD (shown as the radius from the quadrant center), and NCRMSE (shown as the radius from the expected point, which is located at the point where *R* and NSD are unity).

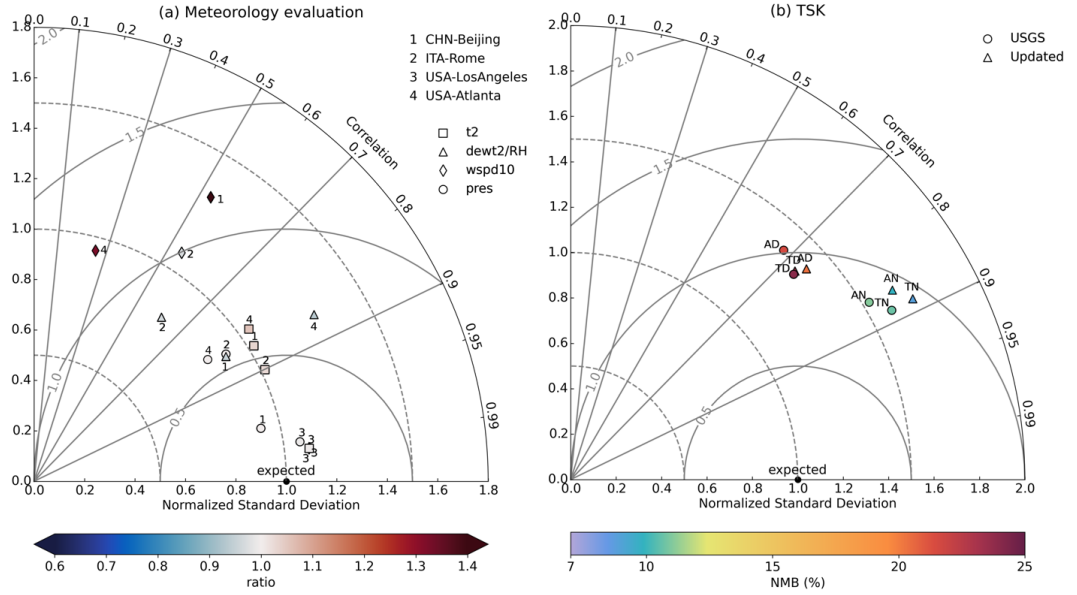

Figure 2. Taylor Diagrams for evaluating UI-WRF-Chem model simulated (a) meteorological variables (t2, dewt2 or RH, wspd10 and pres) with ground observations for CHN-Beijing, ITA-Rome, USA-LosAngeles and USA-Atlanta target areas, and (b) surface skin temperature (TSK) with MODIS observed land surface temperature (LST) for CHN-Beijing during July 2018. In (a), evaluation results of daily meteorology variables are based on the model final configuration for each target area (Sect 3). Color bar represents the ratio between model results and ground observations. In (b), USGS and updated refer to the UI-WRF-Chem sensitivity simulations 2N_def (default USGS land cover type and subsequently derived GVF, LAI and albedo) and 2N_upd (updated land cover type, GVF, LAI and albedo with 2018 MODIS land data) in Table 1, respectively. UI-WRF-Chem simulated TSK averaged over the Terra and Aqua overpass time during daytime (TD and AD) and nighttime (TN and AN), respectively are compared to the corresponding Terra and Aqua observations. Color bar represents the normalized mean bias (NMB) between model results and satellite observations.

https://doi.org/10.5194/egusphere-2025-1360
Preprint. Discussion started: 5 May 2025

There are many physics schemes that can be used in WRF-Chem. We select the commonly used schemes for each target area based on literature review and our previous work (e.g. (Yang et al., 2013; Sha et al., 2021; Zhang et al., 2022)). We also consider a few other factors as described below. For the cumulus scheme, we consider the Grell 3D ensemble (G3D, (Grell and Dévényi, 2002)) scheme, which also accounts for cloud radiation feedback. With the current version of the code, regardless of which cumulus scheme is used, the chemistry will be transported using the G3D scheme while other scalars are transported with the selected cumulus scheme. Therefore, the G3D scheme is used to ensure the consistency between chemistry and physics. For model spatial grids greater than 10 km, they usually rely on the cumulus parameterization to determine the subgrid convective processes. For model spatial grids smaller than 10 km, it is generally considered as the convective gray zone, where the use of convective parameterization or explicit resolving treatment of the convective process remains to be an ongoing question (Jeworrek et al., 2019). Typically, for model spatial grids larger than 5 km, convective parameterization has been used in regional model studies (e.g. (Zhang and Mcfarlane, 1995; Clark et al., 2009; Dudhia, 2014)). For model spatial grids smaller than 5 km, generally considered convection-permitting scale, numerous regional model studies have suggested to turn off the cumulus scheme (e.g. (Prein et al., 2015; Wang et al., 2021b; Weisman et al., 1997; Weisman et al., 2008; Done et al., 2004; Gao et al., 2017)), especially if the cumulus scheme is not scale-aware (Wagner et al., 2018). Therefore, we have chosen to turn off the cumulus scheme here for the inner domain (D2) with the 4 km spatial resolution. Future work will explore the use of a scale-aware cumulus schemes such as the Grell-Freitas scheme (GF, (Grell and Freitas, 2014)) after incorporating the fix of including transport of the chemistry by the GF scheme when GF is selected, as described by Li et al. (2018, 2019).

For the microphysics scheme, an inexpensive scheme is typically sufficient for model spatial grids greater than 10 km but a more complex scheme that accounts for the prediction of the mixed phases (6-class schemes, including graupel) and number concentrations (double-moment schemes) is required (Han et al., 2019). Therefore, we consider these three schemes in the current work: the Lin scheme (Lin et al., 1983; Chen and Sun, 2002), the WRF Single-Moment 6-Class Microphysics Scheme (WSM6) (Hong and Lim, 2006) and the Morrison scheme (Morrison et al., 2009). The former two is a single-moment 6 class scheme and the latter one is a double-moment scheme, which also predicts the number concentration of the hydrometer besides the total amount. All of the three schemes include the simulations of graupel which is shown to help with the simulation of convection for higher resolution simulation (Brisson et al., 2015). At convective-permitting scales, the graupel size representation could play a more important role in the precipitation prediction than the number of moments (single .vs. double) in certain cases (Adams-Selin et al., 2013).

For the shortwave radiation scheme, we only consider the two-stream multiband Goddard scheme (Chou et al., 1998) and the Rapid Radiative Transfer Model for GCMs (RRTMG) (Iacono et al., 2008), which both include the direct aerosol radiation feedback. For the longwave radiation, we

https://doi.org/10.5194/egusphere-2025-1360
Preprint. Discussion started: 5 May 2025

select the RRTMG and the Rapid Radiative Transfer Model (RRTM) schemes (Mlawer et al., 1997). RRTMG for both shortwave and longwave radiation schemes are recommended to pair together in the model by the developing team of WRF-Chem. For the planetary boundary layer (PBL) scheme and the corresponding surface layer scheme, we consider the nonlocal boundary layer scheme – the Yonsei University scheme (YSU, (Hong et al., 2006)) with the revised fifth-generation Pennsylvania State University – National Center for Atmospheric Research Mesoscale Model (MM5) (Grell et al., 1994; Jiménez et al., 2012) surface layer scheme. We also consider two commonly used local boundary layer schemes: Mellor-Yamada-Janjic (MYJ, (Janjic, 2001)) with the ETA similarity surface layer scheme; Mellor-Yamada-Nakanishi-Niino level 2.5 (MYNN2.5, (Nakanishi and Niino, 2004)) with the MYNN surface layer scheme. When using the YSU scheme, we also turn on the surface drag parameterization (Jiménez and Dudhia, 2012) to improve topographic effects on surface winds over complex terrain. The land surface model is the Noah land model (Chen and Dudhia, 2001), which incorporates our updates of the land surface properties as described in Sect 2.2. Additionally, for a specific target area, other physics schemes not mentioned here but commonly used in that area will also be tested.

Details regarding the selection and evaluation results of the physics scheme for the four target areas are available in Text S2 of the SI. Here, we provide a summary of the evaluation results. Sensitivity simulations performed for each target area are listed in Table S1 and we focus on the testing of the following schemes: microphysics, shortwave and longwave radiation and PBL. We evaluate four UI-WRF-Chem simulated meteorology variables with surface observations: air temperature at 2m (t2), dew temperature at 2m (dewt2) or relative humidity (RH), wind speed at 10m (wspd10) and sea level pressure (pres). Results of the hourly or 3-hourly evaluation of the meteorology variables are summarized in Table S2 and Fig S1. Overall, all the sensitivity simulations of t2 and pres for all the target areas show the highest correlation (> 0.8). Dewt2 or RH also show good correlation (0.59 – 0.84) with ITA-Rome showing the lowest correlation. The case study of ITA-Rome is conducted over June 2023, where some areas in Italy experienced rainfall events about one third of the month. Uncertainties of UI-WRF-Chem capturing the rainfall events (discussed in Sect 4.2) could result in the lower correlation of RH. Comparatively, wspd10 shows lower correlation (0.22 – 0.52) with USA-Atlanta showing the lowest correlation. Across the target areas, we find that wspd10 is most sensitive to PBL scheme compared with other schemes tested, which is also found in previous studies (e.g. (Yu et al., 2022)). It is found that no single combination of the physics scheme will result in the best performance for each meteorology variable evaluated. The interaction of these different parametrized processes mentioned above (e.g. convection, boundary layer mixing, microphysics and radiation) are complex (Prein et al., 2015) and it is region, case and variable specific. Therefore, model performance can vary from region to region or case to case.

Based on the evaluation results, we select the optimal combination of various physics schemes tested as the final configuration for each target area. Since MAIA will use daily averaged data for product generation, we also summarize the statistics of the evaluation of the daily meteorology

https://doi.org/10.5194/egusphere-2025-1360
Preprint. Discussion started: 5 May 2025

variables for the four target areas in Fig 2(a), for the final configuration only. We find that UI-WRF-Chem simulated daily t2, dewt2 and pres all show high correlation (> 0.7) and low NMB ((–10%) – (+ 10%)) across the target areas. For evaluation of daily wspd10, correlation increases, and bias decreases compared with hourly evaluation. For USA-Atlanta, the daily wspd10 still shows lower correlation (~0.25) compared with other target areas. The sensitivity simulation of USA-Atlanta is conducted over June 2022 and majority of the wspd10 are under 5 m s^{-1}. It can be challenging for the model to capture this stable condition very well. Future work could focus on trying nudging with ground observation to improve the model performance over this area. We also recognize that our sensitivity tests are limited to one month for each target area. We are not able to test the performance for different seasons. Nevertheless, it provides values for understanding the model sensitivity to different schemes at different locations.

Biogenic emissions for VOCs are from the MEGAN scheme and soil NO_x emissions are from the BDISNP scheme. Fire emissions are from the FLAMBE emission inventory and dust emissions use the GOCART with AFWA modification. Here, we use MEIC 2016 as the anthropogenic emission for CHN-Beijing and NEI 2017 emission inventory for USA-LosAngeles and USA-Atlanta. The HTAP_v3 2018 is used for ITA-Rome. The gas phase chemistry is the RADM2, and the aerosol module is the newly added scheme MADE/SORGAM-DustSS: the MADE/SORGAM scheme with the addition of dust and sea salt aerosol species as described in Sect 2.4.

4. Case studies for different target areas

4.1 Case study – CHN-Beijing

Beijing and its surrounding area in China, are affected by both local and regional emissions as well as long-range transport (Wu et al., 2021; Zhang et al., 2018). In recent decades, the North China Plain including the Beijing area has experienced severe PM pollution problems as a result of the rapid economic growth and urbanization (Zhang et al., 2016). In addition to the impacts of anthropogenic emission on surface PM levels, strong dust storms from the Taklamakan Desert and the Gobi Desert sometimes can be transported downwind to the Beijing area and affect local air quality in the springtime. Here for the CHN-Beijing target area (Fig 1(a)), we first focus on a dust intrusion event during 24–31 March 2018, to study the impacts of chemical boundary conditions on surface PM. Figure 3 shows the MODIS Aqua observed AOD over part of China for the period of this event. The dust storm can be seen on 26 March 2018, at both the Taklamakan and Gobi Deserts and by 28 March, strong dust clouds have been transported to Beijing and its surrounding areas. Figure S2 displays the movement of surface observations of daily PM_{10} mass concentration across China from 24 March to 31 March 2018. On 27 March and 28 March 2018, high surface PM_{10} concentration were observed in Beijing, Tianjin and Hebei province with hourly concentration exceeding 1000 μg m^{-3} (not shown here). Then, we focus on July 2018 to study the impacts of updating land surface properties and soil NO_x emission scheme on model performances.

https://doi.org/10.5194/egusphere-2025-1360
Preprint. Discussion started: 5 May 2025

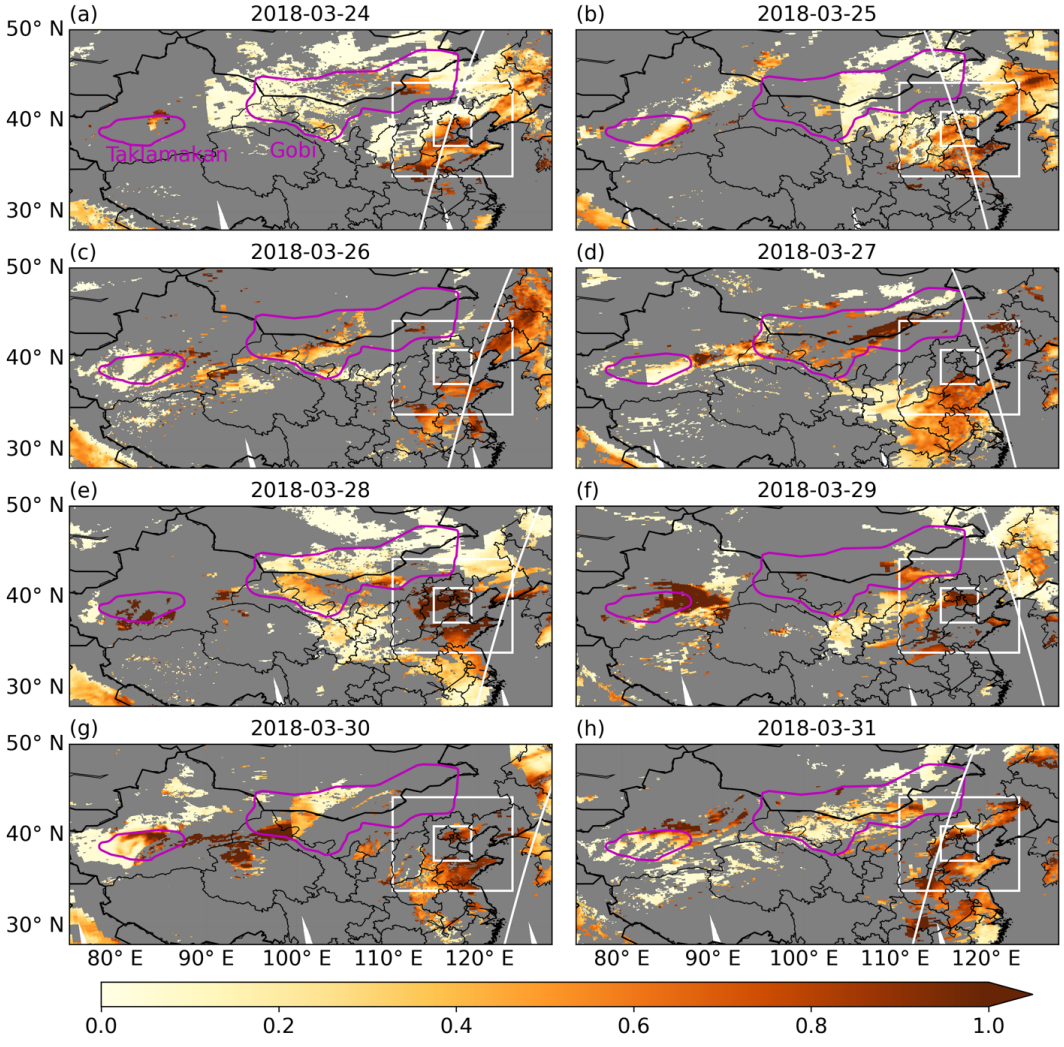

Figure 3. (a)–(h) MODIS Aqua Deep Blue (DB) AOD from 24–31 March 2018. The white boxes represent the UI-WRF-Chem 2 nested domains for outer (D1) and inner domain (D2) over CHN-Beijing, respectively. The white diagonal lines indicate the CALIOP tracks. The magenta contour lines represent the Taklamakan and Gobi Deserts.

4.1.1 Sensitivity experiment design

For CHN-Beijing target area, we carry out a suite of sensitivity simulations using the UI-WRF-Chem framework as shown in Table 1 to investigate the impacts of chemical boundary conditions,

https://doi.org/10.5194/egusphere-2025-1360
Preprint. Discussion started: 5 May 2025

630 updated land surface properties and soil NO_x emission scheme on model performance. First, three simulations are conducted during March 2018 to study the impacts of using MERRA-2 data to provide chemical boundary conditions on model performance. Additionally, four simulations are carried out for July 2018 to investigate the impacts of updating land surface properties as well as surface soil NO_x emission scheme. The simulation with "2N_def" uses the default USGS land
635 cover type and subsequently derived GVF, LAI and albedo, using a predefined look-up table. The simulations with "2N_upd" uses the corresponding updated land cover type, GVF, LAI and albedo, based on the 2018 MODIS land data products for the simulation period, as described in Sect 2.2. The simulations with "2N_*_snox*" use our newly developed BDISNP soil NO_x emission scheme.

640 Table 1. A suite of UI-WRF-Chem sensitivity simulations with different chemical boundary conditions, land data and soil NO_x emission schemes for CHN-Beijing.

simulation name[a]	land data[b]	soil NO_x emission[c]	species considered in the chemical boundary[d]	simulation time[e]
2N_upd_snox-none	updated	BDISNP	none	03/2018
2N_upd_snox-dust	updated	BDISNP	dust + other aerosols	03/2018
2N_upd_snox-dust PSD	updated	BDISNP	dust PSD + other aerosols	03/2018
2N_def	USGS	Guenther	dust + other aerosols	07/2028
2N_upd	updated	Guenther	dust + other aerosols	07/2018
2N_upd_MEGAN	updated	MEGAN	dust + other aerosols	07/2018
2N_upd_BDISNP	updated	BDISNP	dust + other aerosols	07/2018

[a]The simulation name starting with "2N*" refers to the 2 nested domains used for CHN-Beijing as shown in Fig 1(a). The 2 nested domains have a horizontal spatial resolution of 4 km x 4 km and 12 km x 12 km for the inner and outer domain, respectively.

[b]We test different land surface properties used for the UI-WRF-Chem static input data. The simulation name with "*def*" refers
645 to the use of USGS land cover type data and subsequently derived GVF, LAI and albedo, with a predefined look-up table. The simulation name with "*upd*" refers to the use of updated land cover type, GVF, LAI and albedo data with 2018 MODIS land data products.

[c]We test different soil NO_x emission schemes. The Guenther scheme calculates biogenic emissions including soil NO_x emissions, without any external input datasets needed. The MEGAN scheme requires external input files to calculate biogenic emissions
650 including soil NO_x emissions. The BDISNP is our newly developed scheme. Since the USGS land data is only compatible with the Guenther scheme, we conduct sensitivity simulations "2N_def" and "2N_upd" to evaluate the impacts of updating land surface properties. The simulation name with "*snox*" means that the BDISNP soil NO_x emission scheme is used.

[d]We test different scenarios of chemical species used in MERRA-2 data for updating UI-WRF-Chem chemical boundary conditions. "None" (simulation name with "*none*") means that chemical boundary conditions from MERRA-2 data are not used.
655 "dust + other aerosols" (simulation name with "*dust*") means that dust and other aerosols including sulfate, BC and OC are considered in the chemical boundary conditions from MERRA-2 data. "dust particle size distribution (PSD) + other aerosols" (simulation name with "*dust PSD*") is the same as "dust + other aerosols" except that we use the ratio of averaged PSD from AERONET observations and MERRA-2 data over 2000–2020 to scale the dust concentration for each size bin in the MERRA-2 data. More details can be found in Sect 4.1.1.

660 [e]We conduct the sensitivity simulations in two different time periods: March and July 2018, respectively. The simulations in March focus on evaluating the impacts of using MERRA-2 data to provide chemical boundary conditions on model performance while the simulations in July focus on the impacts of updating land surface properties with MODIS data and soil NO_x emission scheme.

https://doi.org/10.5194/egusphere-2025-1360
Preprint. Discussion started: 5 May 2025

The impacts of chemical boundary conditions are evaluated from several sensitivity experiments. In the simulation "2N_upd_snox-none", no chemical species from MERRA-2 data are transported into the domain. In the simulation "2N_upd_snox-dust", dust and other aerosols including sulfate, BC and OC are considered in the chemical boundary condition from MERRA-2 data. Furthermore, to constrain the chemical boundary condition for the allocation of dust concentration as a function of different size bins, we analyze the AERONET measured aerosol volume size distribution (AVSD) data from 2000 to 2020. If the fine mode fraction (FMF) of AOD at 500 nm is less than 0.3 (Lee et al., 2017), it is considered as a dust event. Figure 4(a) shows the averaged dust particle size distribution (PSD) over the AERONET sites between 2000–2020 from both AERONET and MERRA-2 data for all the dust events that occurred in CHN-Beijing. The ratio between the mean of the AERONET PSD and MERRA-2 PSD for each of the five dust size bins is then used as a constraint to scale the dust concentration in each bin in the MERRA-2 chemical boundary data. The sensitivity run "2N_upd_snox-dust PSD" in Table 1 is based on this result.

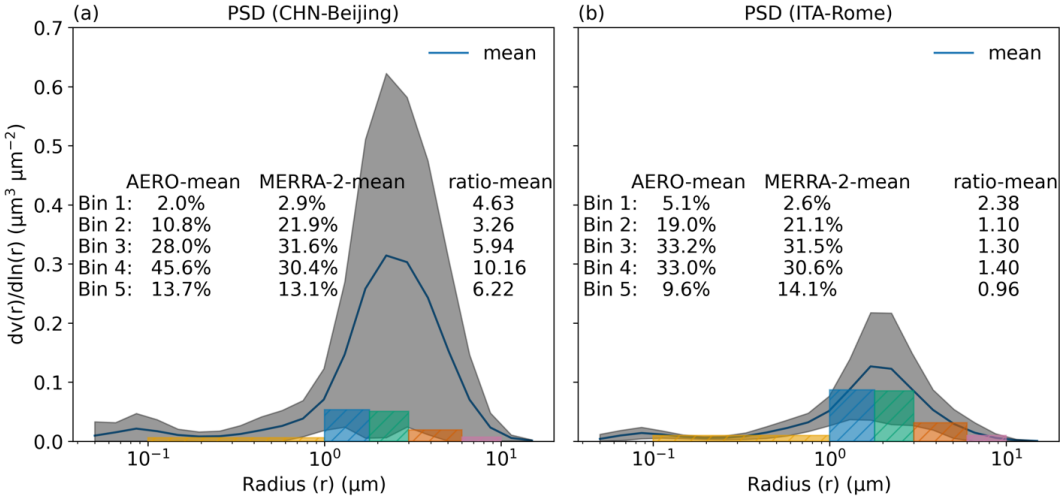

Figure 4. Averaged particle size distribution (PSD) from AERONET observations (blue line) and MERRA-2 data (the 5 colored bins) for (a) CHN-Beijing and (b) ITA_Rome over 2000–2020 and 2000–2023, respectively. The AERONET sites used are shown as the stars in Fig 1(a) and (b), respectively. The dark gray areas represent the AERONET variability. AERO-mean and MERRA-2 mean represent the fraction of the PSD from each bin over the sum of the 5 bins. Ratio-mean is the ratio of the total PSD of AERONET over MERRA-2 for each bin.

Three UI-WRF-Chem sensitivity simulations in Table 1 are run from 18 March to 31 March 2018, for evaluating the impacts of using MERRA-2 data to provide chemical boundary conditions. The simulation results with the first 6 days are used as initialization. Model output from 24 March to 31 March 2018, are used for analysis, unless noted otherwise. The rest of the four simulations are used for evaluating the impacts of updating land surface properties and soil NO_x emission scheme on model performance. They are carried out from 24 June to 31 July 2018, and model outputs from

https://doi.org/10.5194/egusphere-2025-1360
Preprint. Discussion started: 5 May 2025

1 July to 31 July are used for data analysis. We mainly use model output from the inner domain (D2) for data analysis unless noted otherwise.

4.1.2 Impacts of chemical boundary conditions on surface PM and AOD

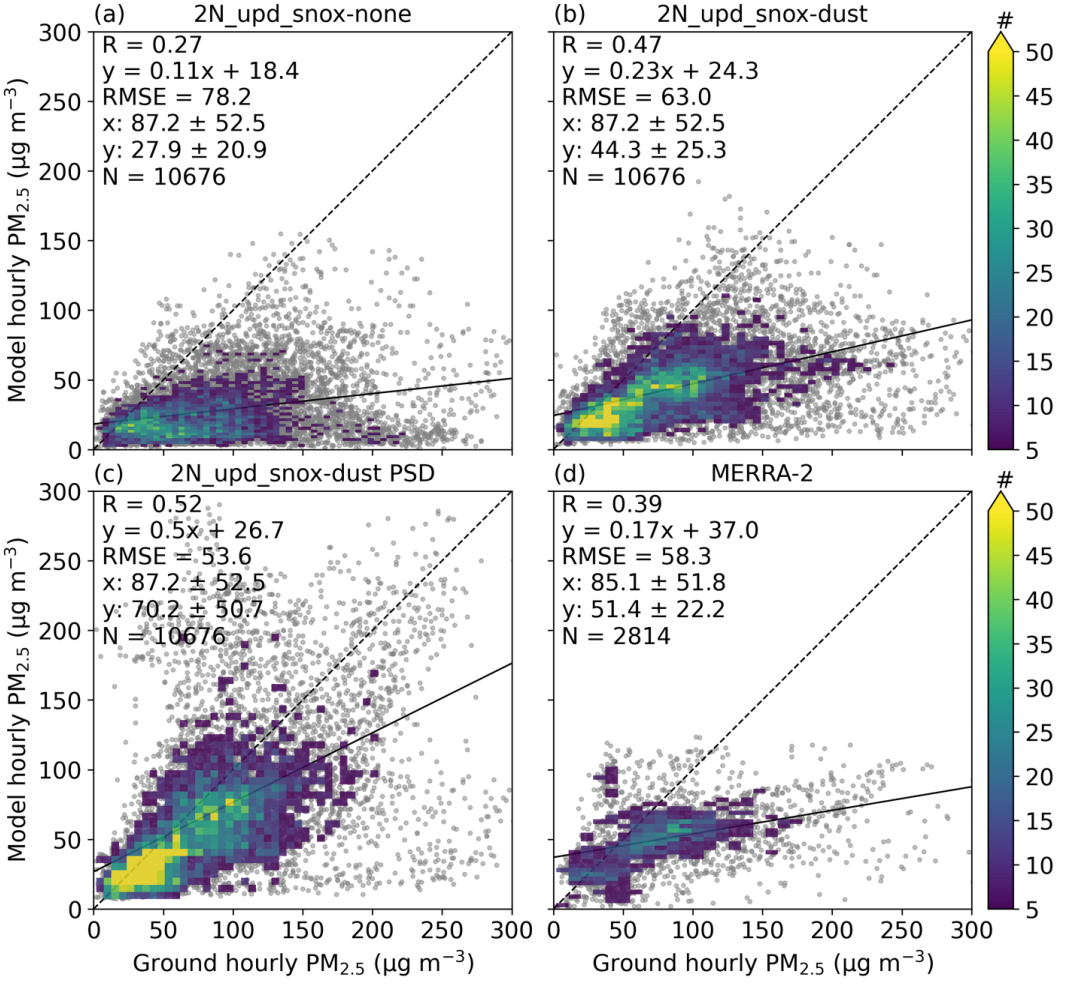

Figure 5. Scatter plot of hourly surface $PM_{2.5}$ concentration between model (y axis) and ground observation (x axis) for surface sites in the inner domain (D2) of CHN-Beijing for 24–31 March 2018. (a)–(c) refer to the UI-WRF-Chem sensitivity simulations with different chemical boundary conditions being considered using MERRA-2 data (Table 1). (a) no chemical species, (b) dust and other aerosols and (c) same as (b) except that the dust concentration is scaled based on constraining MERRA-2 dust PSD data with AERONET PSD climatology data. (d) is from MERRA-2 simulated surface $PM_{2.5}$ concentration. Also shown on the scatter plot is the correlation coefficient (R), the root-mean-square error (RMSE), the mean ± standard deviation for observed (x)

https://doi.org/10.5194/egusphere-2025-1360
Preprint. Discussion started: 5 May 2025

and model-simulated surface $PM_{2.5}$ (y), the number of collocated data points (N), the density of points (the color bar), the best fit linear regression (the solid black line) and the 1:1 line (the dashed black line).

First, we evaluate the effectiveness of using MERRA-2 data to provide chemical boundary conditions in capturing this dust long-range transport event in spring 2018. Figure 5 shows the overall evaluation of model simulated hourly surface $PM_{2.5}$ mass concentration against ground observations over PTA-Beijing during 24–31 March 2018. Results are presented for three sensitivity experiments, as described in section 4.1.1. Without considering any chemical species in the boundary, the UI-WRF-Chem simulated $PM_{2.5}$ concentration (2N_upd_snox_none) underestimates ground observations with a MB of −59.3 μg m^{-3}. After including dust and other aerosols in the boundary conditions, the UI-WRF-Chem simulated $PM_{2.5}$ concentration (2N_upd_snox_dust) increases from 27.9 μg m^{-3} to 44.3 μg m^{-3} and thus reduces the MB to −42.9 μg m^{-3}. Correlation (*R*) also improves with an increase from 0.27 to 0.47. By constraining the dust PSD in the MERRA-2 data with the climatology data from AERONET, the UI-WRF-Chem simulated $PM_{2.5}$ (2N_upd_snox_dust PSD) further improves the model performance with MB of −17 μg m^{-3} and *R* of 0.52. It also outperforms the MERRA-2 simulated surface $PM_{2.5}$ concentration (MB of −33.7 μg m^{-3} and *R* of 0.39).

Figure 6(a) and Figure S3 show the time series of hourly surface $PM_{2.5}$ and PM_{10} concentration from 24–31 March 2018 for both model simulations and ground observations. During 27–28 March, when the dust front intruded PTA-Beijing, hourly observations of surface $PM_{2.5}$ and PM_{10} concentration averaged over all the sites could reach approximately 150 and 900 μg m^{-3}, respectively. The UI-WRF-Chem simulation without chemical boundary conditions (2N_upd_snox_none) misses this peak for both $PM_{2.5}$ and PM_{10} while both the UI-WRF-Chem simulation with chemical boundary condition (2N_upd_snox_dust) and MERRA-2 data capture this peak for $PM_{2.5}$ but miss the peak for PM_{10}. The UI-WRF-Chem simulation with dust PSD constrained (2N_upd_snox_dust PSD) capture both the peak of $PM_{2.5}$ and PM_{10}. Compared with the simulation without boundary conditions (2N_upd_snox_none), adding chemical boundary conditions (2N_upd_snox_dust) improves model performance with increased correlation for both $PM_{2.5}$ (0.41 to 0.72) and PM_{10} (0.06 to 0.23). The simulation with dust PSD constrained (2N_upd_snox_dust PSD) does not improve the correlation of $PM_{2.5}$ (0.65) but does for PM_{10} (0.28), compared with the simulation using dust in the chemical boundary (2N_upd_snox_dust).

Not only does considering chemical boundary conditions improve surface PM mass concentration, it also helps with the total aerosol column amount and vertical distribution. First, Figure 6(b)–(d) shows the AOD evaluation between model simulations and AERONET observations. Without considering boundary conditions, the UI-WRF-Chem simulation (2N_upd_snox_none, 0.05) significantly underestimates the AERONET observed AOD (0.73) and shows poor correlation (0.02). Including dust and other aerosols (2N_upd_snox_dust) enhances UI-WRF-Chem simulated AOD (0.29) and correlation (0.79). Overall, constraining the dust in the boundary

https://doi.org/10.5194/egusphere-2025-1360
Preprint. Discussion started: 5 May 2025

(2N_upd_snox_dust PSD) shows the best performance with simulated AOD of 0.93 and correlation of 0.83.

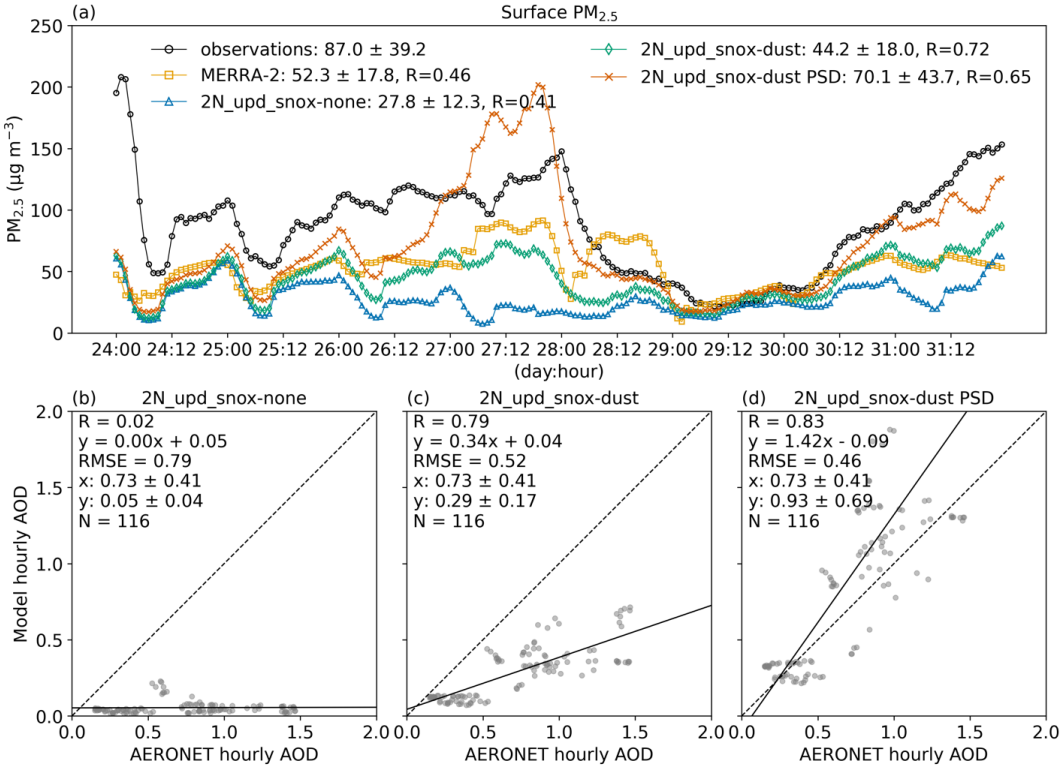

Figure 6. (a) time series of hourly surface $PM_{2.5}$ concentration averaged over surface sites in the inner domain (D2) of CHN-Beijing for 24–31 March 2018, from model simulations and ground observations. 2N_upd_snox-none/dust/dust PSD refer to the UI-WRF-Chem sensitivity simulations with different chemical boundary conditions being considered using MERRA-2 data (Table 1): no chemical species; dust and other aerosols; dust concentration is scaled based on constraining MERRA-2 dust PSD data with AERONET PSD climatology data. Also shown on the plot is the mean ± standard deviation of surface $PM_{2.5}$ for model simulations or observations as well as the correlation coefficient (R). (b)–(d): scatter plot of hourly AOD between model (y axis) and AERONET observation (x axis) for 24–31 March 2018. Also shown on the scatter plot is R, the root-mean-square error (RMSE), the mean ± standard deviation for observed (x) and model-simulated AOD (y), the number of collocated data points (N), the best fit linear regression (the solid black line) and the 1:1 line (the dashed black line).

We then compare the UI-WRF-Chem simulated vertical aerosol profile with the Cloud-Aerosol Lidar with Orthogonal Polarization (CALIOP) data for the outer domain (D1) during 26–28 March, when dust reaches the PTA-Beijing domain. Figure 7 shows the CALIOP derived aerosol extinction coefficient, aerosol type as well as UI-WRF-Chem simulated extinction coefficient. The CALIOP ground tracks are located within the UI-WRF-Chem outer domain (D1) (Fig 3) and model grids that overlap with the tracks are selected. From both the CALIOP aerosol extinction

https://doi.org/10.5194/egusphere-2025-1360
Preprint. Discussion started: 5 May 2025

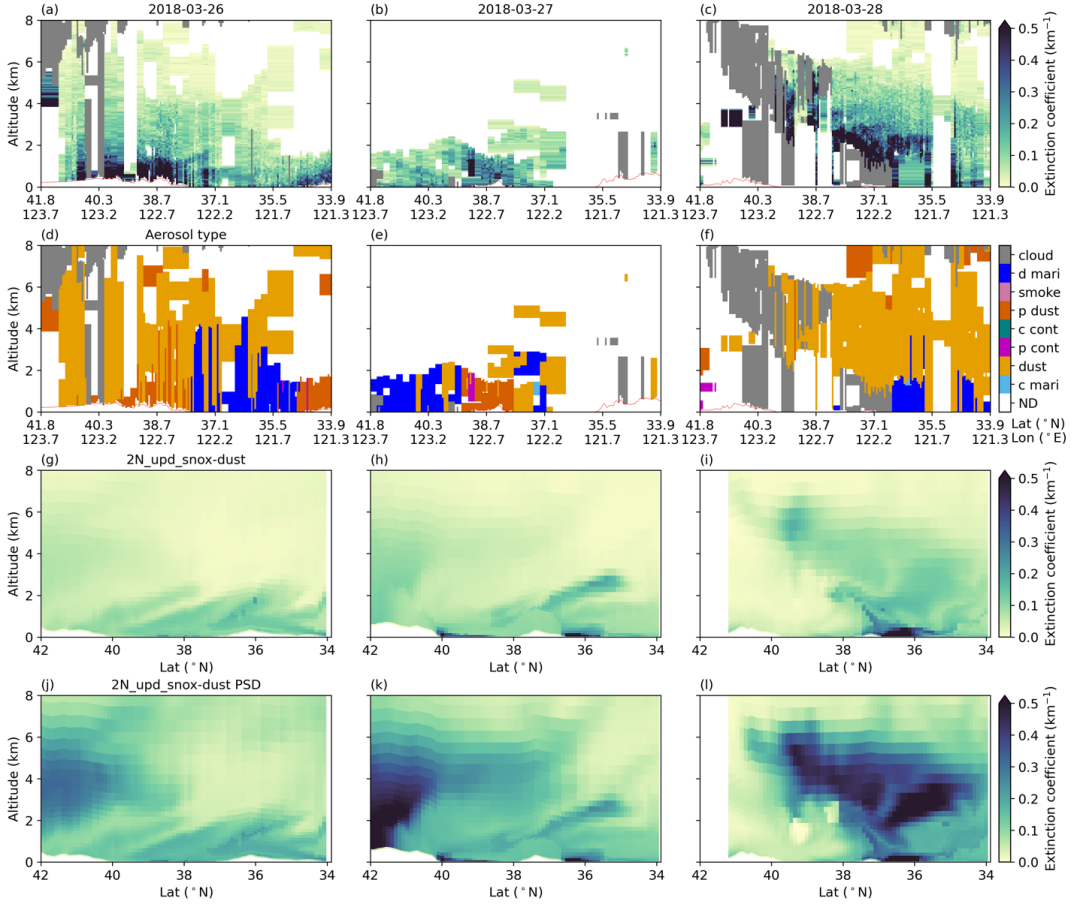

Figure 7. Comparison of CALIOP–derived vertical profile of aerosol extinction coefficient (532 nm, (a)–(c)) and aerosol type ((d)–(f)) with UI-WRF-Chem simulated extinction coefficient for CHN-Beijing over 26–28 March 2018. UI-WRF-Chem outputs are from the outer domain (D1) that overlap with CALIOP tracks (Fig 3). (g)–(i) are the extinction coefficients from the UI-WRF-Chem sensitivity simulation 2N_upd_snox-dust, where dust and other aerosols are considered in the MERRA-2 chemical boundary conditions. (j)–(l) are the extinction coefficients from UI-WRF-Chem sensitivity simulation 2N_upd_snox-dust PSD where dust concentration is scaled in the MERRA-2 chemical boundary conditions, based on constraining MERRA-2 dust PSD data with AERONET PSD climatology data. In (a)–(f), the gray areas represent cloud. In (d)–(f), different aerosol types are classified: d mari for dusty marine, p dust for polluted dust, c cont for clean continental, p cont for polluted continental, c mari for clean marine. ND includes areas that have clean air and aerosol type not being determined.

coefficient and aerosol type, we can see that dust is dominating the vertical distribution above ~3–4 km and mixed with marine and anthropogenic aerosols in the boundary layer. Without considering aerosols in the chemical boundary conditions, the UI-WRF-Chem simulated extinction coefficient is negligible above the boundary layer (not shown here). After considering

https://doi.org/10.5194/egusphere-2025-1360
Preprint. Discussion started: 5 May 2025

dust and other aerosols in the chemical boundary conditions, we can see the increase in the extinction coefficient in the vertical distribution (Fig 7(g)–(i)). Constraining the dust in the boundary (2N_upd_snox_dust PSD, Fig 7(j)–(l)) further enhances the vertical distribution of the aerosol extinction coefficient, which matches better with the CALIOP observations. This reflects the effectiveness of including dust and other aerosols in the chemical boundary condition to better capture the vertical distribution of aerosol properties in this dust intrusion event. We note that CALIOP data is also subject to uncertainties of the lidar ratio used in deriving the extinction, and so is the extinction modeled by UI-WRF-Chem (Yang et al., 2013). Hence, CALIOP data is used as a relative reference to assess the model improvement.

Since PTA-Being is located downwind of the dust source regions in this case, there could be uncertainties in simulating the transport of different dust size bins in MERRA-2 data from source regions. Thus, our constraining method could provide an effective way to improve the dust size distribution in the boundary conditions and subsequently improve model simulated surface PM concentration as well as vertical distribution of aerosols. This method could also benefit other PTAs such as ITA-Rome, that can be affected by dust transport events, which will be discussed in Sect 4.2.

4.1.3 Impacts of updated land surface properties on model performance

The UI-WRF-Chem model simulated surface skin temperature (TSK) is evaluated with satellite observations of land surface temperature (LST) from MODIS onboard Terra and Aqua for July 2018. We first regrid the MODIS daily LST data into the WRF-Chem model grids. The Beijing-Tian-Hebei region is one of the highly urbanized clusters in the world and has experienced intense urban heat island (UHI) effects in the past decade (Wang et al., 2016; Clinton and Gong, 2013). First, by comparing the default and updated land cover type (Fig 8(a) and Fig 8(f)), we can see that the updated land cover type captures the urban growth over the region. The corresponding land surface properties including LAI, GVF and albedo also show changes with the updated data (Fig S4). Both daytime (~10:30 am and ~1:30 pm LT) (Fig 8(b) and Fig S5(a)) and nighttime (~10:30 pm and ~1:30 am LT) (Fig 8(g) and Fig S5(e)) LST from MODIS Terra and Aqua show the UHI phenomenon over the region. Our UI-WRF-Chem model simulated TSK with updated land surface properties can capture the UHI spatial pattern with higher temperature in urban areas than rural areas for both daytime and nighttime. It matches the spatial pattern of satellite observed LST UHI better than the UI-WRF-Chem simulation with use of the default USGS land cover type and other surface properties, which is consistent with our previous work (Wang et al., 2023). Figure 2(b) shows the Taylor Diagram of comparing UI-WRF-Chem simulated LST with MODIS Terra and Aqua daytime and nighttime, respectively. We find that the UI-WRF-Chem simulated TSK with updated land surface properties decreases the relative bias for both Terra and Aqua daytime and nighttime, compared with the UI-WRF-Chem simulation using the default USGS land surface properties. The model simulated TSK with updated land surface properties also results in an

https://doi.org/10.5194/egusphere-2025-1360
Preprint. Discussion started: 5 May 2025

increase in correlation for the Aqua daytime period compared with the model simulation using the USGS land surface properties.

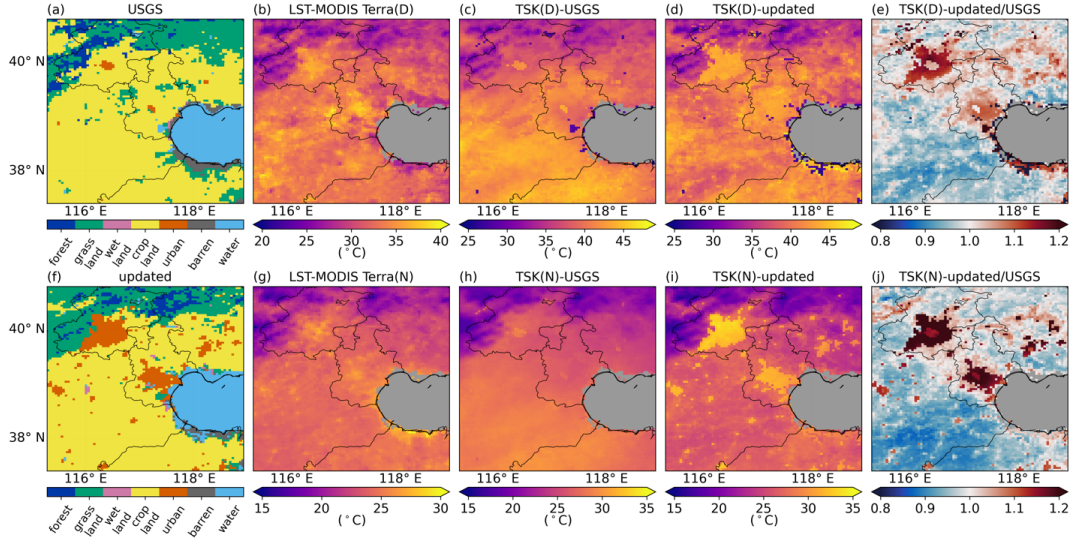

Figure 8. Comparison of UI-WRF-Chem simulated surface skin temperature (TSK) with MODIS Terra observed land surface temperature (LST) for CHN-Beijing in July 2018. (a) and (f) are the land cover type from the default USGS data and the updated data with 2018 MODIS land data. (b) and (g) are the MODIS Terra LST during daytime (D) and nighttime (N), respectively. (c) and (d) are model simulated TSK averaged over Terra overpass time during daytime from UI-WRF-Chem sensitivity simulations 2N_def (default USGS land cover type and subsequently derived GVF, LAI and albedo) and 2N_upd (updated land cover type, GVF, LAI and albedo with 2018 MODIS land data) in Table 1, respectively. (e) is the ratio between (d) and (c). (h)–(j) are the same as (c)–(e) but averaged over Terra overpass time during nighttime. Oceans are masked as grey colors on the plots for (b)–(e) and (g)–(j).

Figure S6 shows the potential impacts of updated land surface properties on model simulated planetary boundary layer height (PBLH) and subsequently on surface $PM_{2.5}$ concentration. We find that the PBLH mainly increases in the urban areas where the land surface temperature increases, which in turn leads to a decrease in surface $PM_{2.5}$. Our work shows the promising use of updated land surface properties with timely satellite data to better capture the land cover type and other land surface properties for areas with fast urban development. To better study the impacts of UHI in the region, urban canopy model could be used to include more details about the underlying urban surface feature and better simulate the physical processes in the boundary layer (He et al., 2019; Liang et al., 2021) with a finer spatial resolution, which is beyond the scope of the current work.

https://doi.org/10.5194/egusphere-2025-1360
Preprint. Discussion started: 5 May 2025

4.1.4 Impacts of updated soil NO_x emission scheme on model performance

Our previous work (Sha et al., 2021) has shown the improvement of model simulated NO_2 VCD, when evaluated against TROPOMI NO_2 VCD over croplands in California, using the BDISNP soil NO_x emission scheme. Here, we also use TROPOMI NO_2 VCD to evaluate UI-WRF-Chem simulated NO_2 VCD over croplands in the outer domain (D1) of CHN-Beijing for July 2018. Daily TROPOMI NO_2 data are regridded to UI-WRF-Chem grids with averaging kernels being applied. Hourly data from UI-WRF-Chem output, close to the TROPOMI overpass time (~1:30 PM LT) are averaged to compare with TROPOMI data. First, Figure S7 shows the UI-WRF-Chem simulated monthly mean soil NO_x emissions using the default emission scheme – MEGAN (2N_upd_MEGAN in Table 1) and the updated scheme – BDISNP (2N_upd_BDISNP in Table 1), respectively. The MEGAN scheme (Fig S7(a)) simulates low soil NO_x emissions over the whole domain and the BDISNP (Fig S7(b)) instead simulates higher soil NO_x emissions in non-urban areas. Croplands show the largest soil NO_x emissions due to the use of fertilizer.

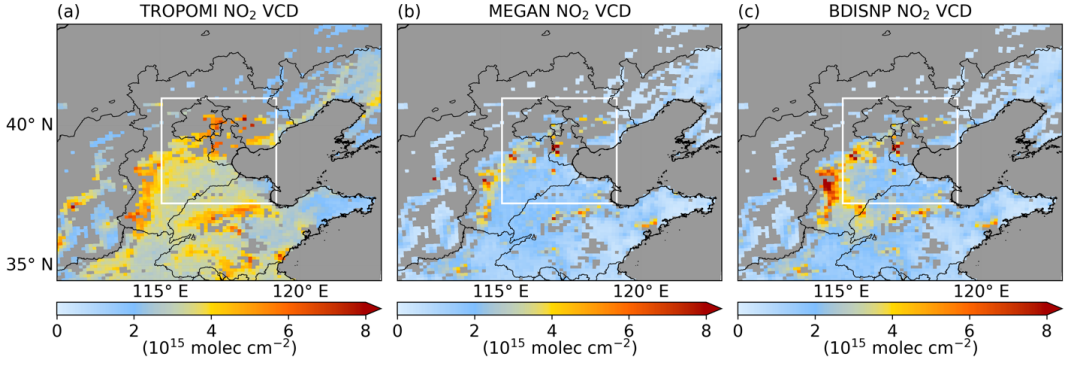

Figure 9. Monthly mean NO_2 tropospheric vertical column density (VCD) over the outer domain (D1) of CHN-Beijing for July 2018 from TROPOMI observation and model sensitivity simulations. Only model grids identified as croplands are shown on the plots. (a) TROPOMI observations; (b) UI-WRF-Chem sensitivity simulation 2N_upd_MEGAN in Table 1 using the MEGAN scheme to calculate soil NO_x emissions; (c) UI-WRF-Chem sensitivity simulation 2N_upd_BDISNP in Table 1 using the BDISNP scheme to calculate soil NO_x emissions. The white box represents the inner domain (D2) of CHN-Beijing.

Then, we compare the model simulated tropospheric NO_2 VCD with TROPOMI NO_2 VCD for July 2018 (Fig 9 and Fig 10). We can find that both simulations underestimate TROPOMI NO_2 VCD (2.2 x 10^{15} molecules cm^{-2}) by 1.4 x 10^{15} and 1.3 x 10^{15} molecules cm^{-2} for the MEGAN and BDISNP respectively (Fig 10(a) and (b)) over the whole domain. Over croplands, we can see the enhancement in the model simulated NO_2 VCD (Fig 9(c)). The model simulated NO_2 VCD increases from 1.4 x 10^{15} using the MEGAN scheme to 1.7 x 10^{15} molecules cm^{-2} using the BDISNP scheme. The BDISNP decreases MAE from 1.59 x 10^{15} molecules cm^{-2} to 1.53 x 10^{15} molecules cm^{-2} over the whole domain mainly due to the improvement over croplands. MAE for croplands decreases from 1.88 x 10^{15} molecules cm^{-2} to 1.77 x 10^{15} molecules cm^{-2} (Fig 10(c) and (d)). The increase in soil NO_x emissions has potential impacts on surface nitrate. Figure S8 shows

https://doi.org/10.5194/egusphere-2025-1360
Preprint. Discussion started: 5 May 2025

that the increase in surface soil NO_x emissions leads to the increase in surface nitrate up to 30% in rural areas. Due to the lack of surface observation of nitrate, we are limited to quantify the impacts of the improvement of soil NO_x emissions on surface nitrate. The MAIA satellite mission coupled with the Geostationary Environment Monitoring Spectrometer (GEMS) (Kim et al., 2020) satellite mission could provide a synergetic opportunity to evaluate both gas and aerosol chemistry.

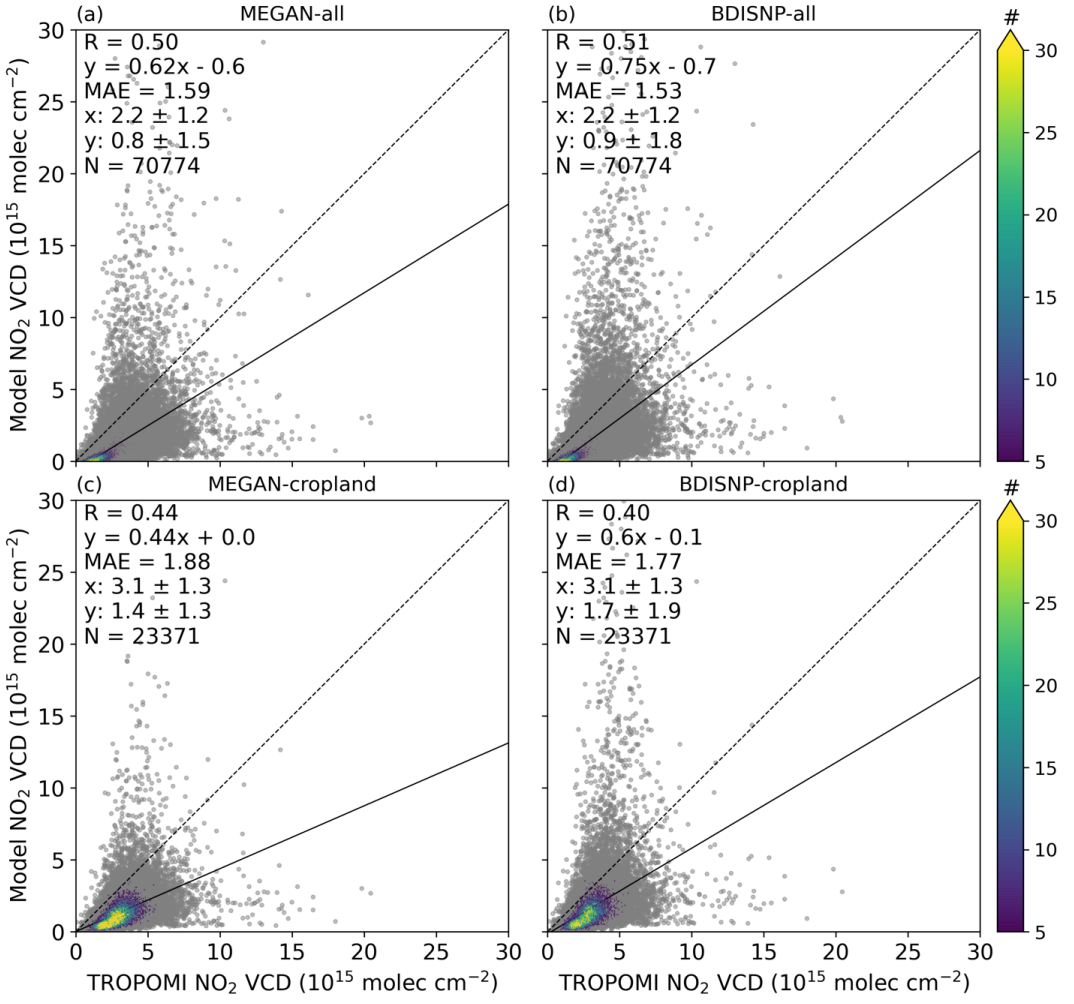

Figure 10. Scatter plot of daily tropospheric NO_2 VCD between model (y axis) and TROPOMI observation (x axis) over the outer domain (D1) of CHN-Beijing for July 2018. (a) and (c) refer to the UI-WRF-Chem sensitivity simulation using the MEGAN scheme (2N_upd_MEGAN in Table 1) and (b) and (d) refer to the sensitivity simulation using the BDISNP scheme (2N_upd_BDISNP in Table 1) to calculate soil NO_x emissions, respectively. (a) and (b) are for model grids over the whole

https://doi.org/10.5194/egusphere-2025-1360
Preprint. Discussion started: 5 May 2025

domain while (c) and (d) are for model grids that are identified as croplands. Also shown on the scatter plot is the correlation coefficient (*R*), the mean absolute error (MAE), the mean ± standard deviation for observed (x) and model-simulated tropospheric NO_2 VCD (y), the number of collocated data points (N), the density of points (the color bar), the best fit linear regression (the solid black line) and the 1:1 line (the dashed black line).

4.2 Case study – ITA-Rome

Our case study over CHN-Beijing target area has demonstrated the benefits of using MERRA-2 data to provide chemical boundary conditions for capturing long-range transport events such as dust intrusion. Some of the other target areas including ITA-Rome are also impacted by dust transport. Saharan dust transport poses a significant concern on air quality in Europe and the Mediterranean Basin. Previous work has shown that Saharan dust outbreaks are more frequent in southern Europe including Italy than northern Europe (Querol et al., 2009; Viana et al., 2014; Pey et al., 2013; Wang et al., 2020a). For example, Pey et al. (2013) showed that across the Mediterranean Basin, African dust outbreaks occurred from 30% to 37% of the annual days in the southern sites and less than 20% of the days in the northern sites. The work of Barnaba et al. (2022) investigated the impacts of African dust on surface PM_{10} concentrations in Italy using surface monitoring sites in Italy from 2006–2012 and found that African dust affected surface PM_{10} levels in Northern and Southern Italy for about 10% and 30% of dates in a year, respectively.

Here, we focus on June 2023, where Saharan dust affected the PM concentration in ITA-Rome, and investigate the benefits of using MERRA-2 data to provide chemical boundary conditions for driving UI-WRF-Chem. For example, one Saharan dust intrusion into Italy occurred from 19–22 June 2023 as seen from the VIIRS AOD (Fig S9) and MERRA-2 simulated dust AOD also captures this dust intrusion event (not shown here). We conduct three UI-WRF-Chem model sensitivity simulations with different chemical boundary conditions to evaluate model simulated surface PM concentration and AOD: (1) simulation "2N-none": no chemical species from MERRA-2 data are transported into the domain; (2) simulation "2N-dust": dust and other aerosols including sulfate, BC and OC are considered in the MERRA-2 chemical boundary condition; (3) simulation "2N-dust PSD": dust concentration of different size bins in the MERRA-2 boundary conditions is constrained using the AERONET PSD climatology data from 2000–2023. AERONET sites close to the Saharan dust source region are used for constraining MERRA-2 PSD (Fig 1(b)). Figure 4(b) shows the averaged PSD over the AERONET sites between 2000–2023 from both MERRA-2 and AERONET data. The ratio between the mean of the AERONET PSD and MERRA-2 PSD for each of the five dust size bins is then used as a constraint to scale the dust concentration in each bin in the MERRA-2 chemical boundary data in the simulation "2N-dust PSD".

Like the case study in CHN-Beijing, using MERRA-2 data to provide chemical boundary conditions for UI-WRF-Chem over ITA-Rome also improves both model simulated surface PM concentration and AOD (Fig 11). Overall, for the whole month of June, the correlation *R* from the sensitivity run 2N-none increases from 0.10 to 0.47, 0.46 to 0.61, and 0.15 to 0.62 for surface $PM_{2.5}$, surface PM_{10} and AOD, respectively compared with the sensitivity simulation 2N-dust. The

https://doi.org/10.5194/egusphere-2025-1360
Preprint. Discussion started: 5 May 2025

MB decreases from –7.2 to –2.5 μg m^{-3}, –14.8 to –2.2 μg m^{-3}, and –0.23 to –0.13 for surface $PM_{2.5}$, PM_{10} and AOD respectively. Using constrained dust concentration in the MERRA-2 data (2N-dust PSD) further reduces the MB for surface $PM_{2.5}$ and AOD and slightly overestimates surface PM_{10}, compared with simulation 2N-dust. In contrast, Both MERRA-2 simulated surface $PM_{2.5}$ and PM_{10} overestimates surface observations with MB of 6.4 μg m^{-3} and 21.8 μg m^{-3}, respectively. UI-WRF-Chem simulated surface $PM_{2.5}$ and PM_{10} have slightly lower correlation than MERRA-2 data but has much lower MB than MERRA-2 data, when evaluated against ground observations. During June 2023, some parts of the ITA-Rome domain experienced precipitation events (Fig S10), which occurred mostly during the first half of the month. Compared to the Global Precipitation Measurement Missions (GPM) observed precipitation and MERRA-2 simulated precipitation (Fig S10), UI-WRF-Chem simulates higher precipitation, which could result in higher wet deposition of aerosols and lower concentration. Figure S11 shows the comparison of model simulated surface daily $PM_{2.5}$ and PM_{10} with ground observations for the first and second half of the month in June 2023, respectively. We can see that UI-WRF-Chem simulation 2N-dust underestimates both surface $PM_{2.5}$ and PM_{10} during the first half of the month (Fig S11(a)–(h)) with MB of –3.0 and –5.5 μg m^{-3}, respectively, while MERRA-2 overestimates surface $PM_{2.5}$ and PM_{10} with MB of 5.1 and 15.7 μg m^{-3}, respectively. During the second half of the month (Fig S11(i)–(p)), UI-WRF-Chem simulation 2N-dust underestimates surface $PM_{2.5}$ with MB of –2.0 μg m^{-3} but slightly overestimates surface PM_{10} with MB of 0.7 μg m^{-3}. MERRA-2 still overestimates surface $PM_{2.5}$ and PM_{10} with MB of 7.4 and 28.4 μg m^{-3}, respectively. Due to the coarse spatial resolution of MERRA-2 data, it may not resolve the localized convective processes well, which could affect the subsequent wet deposition. There are also uncertainties associated with the dust size distribution in MERRA-2 data, which could also play a role in the wet deposition.

Additionally, uncertainty in UI-WRF-Chem model simulated wet deposition of aerosols could also play a role in the model results discussed above. Previous work has mostly focused on dry dust events (e.g. (Zeng et al., 2020)), and less has focused on the wet dust events, especially dust wet deposition. Jung and Shao (2006) implemented a below-cloud dust wet deposition scheme for the UOC dust emission scheme in WRF-Chem. Currently, no dust wet scavenging scheme is implemented for the original GOCART or GOCART AFWA dust scheme in WRF-Chem. As in previous work (Su and Fung, 2015), we have implemented a simple scheme to allow dust wet scavenging by large scale and convective precipitation by assigning a scavenging efficiency for different dust size bins in the model. Future work will focus on implementing a more complex dust wet deposition scheme to better account for the scavenging process that consider the dust particle size distribution etc., such as the work of Tsarpalis et al. (2018) and Zhao et al. (2003). Nevertheless, the case study over ITA-Rome again demonstrates the benefits of using MERRA-2 data to drive UI-WRF-Chem for capturing the dust transport event.

https://doi.org/10.5194/egusphere-2025-1360
Preprint. Discussion started: 5 May 2025

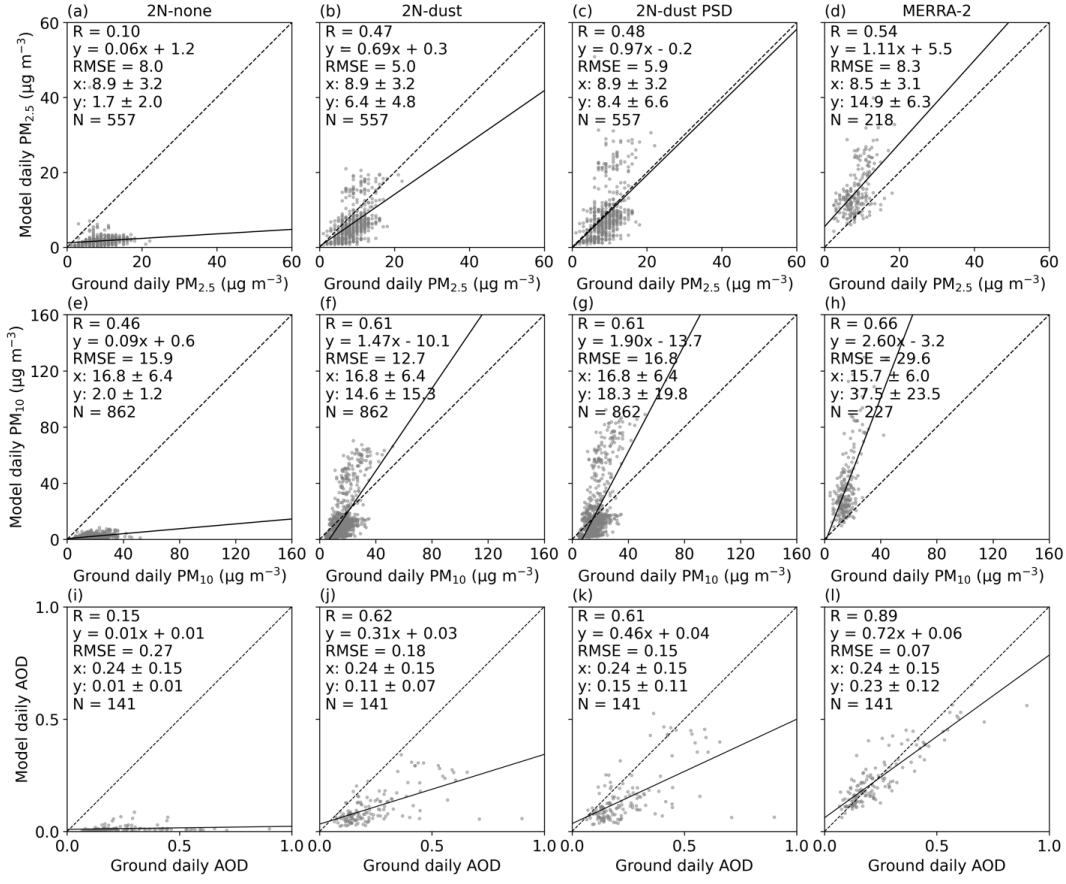

Figure 11. Scatter plot of daily $PM_{2.5}$ concentration ((a)–(d)), PM_{10} concentration ((e)–(h)), and AOD ((i)–(l)), between model (y axis) and ground observation (x axis) over the inner domain (D2) of ITA-Rome for June 2023. (a)–(c), (e)–(g), and (i)–(k) refer to the UI-WRF-Chem sensitivity simulations with different chemical boundary conditions being considered using MERRA-2 data. 2N-none: no chemical species; 2N-dust: dust and other aerosols; 2N-dust PSD: same as 2N-dust except that the dust concentration is scaled based on constraining MERRA-2 dust PSD data with AERONET PSD climatology data. (d), (h) and (l) show the MERRA-2 simulated daily $PM_{2.5}$, PM_{10} and AOD, respectively. Also shown on the scatter plot is the correlation coefficient (*R*), the root-mean-square error (RMSE), the mean ± standard deviation for observed (x) and model-simulated $PM_{2.5}$/PM_{10}/AOD (y), the number of collocated data points (N), the best fit linear regression (the solid black line) and the 1:1 line (the dashed black line).

4.3 Case study – USA-LosAngeles and USA-Atlanta

Each target area has its unique feature of aerosol composition and various factors that affect the aerosol concentration, we have demonstrated the impacts of dust transport on surface PM concentration and AOD over CHN-Beijing and ITA-Rome target areas. Here, we focus on some

https://doi.org/10.5194/egusphere-2025-1360
Preprint. Discussion started: 5 May 2025

fine tuning or testing over USA-Los Angeles and USA-Atlanta target areas to improve the model simulation of surface PM concentration and AOD.

4.3.1 USA-LosAngeles

For the USA-LosAngeles target area (Fig 1(c)), we investigate the impacts of dust emissions on surface PM concentration and AOD. Part of the outer domain (D1) over the USA-LosAngeles target area (here defined as the dust-prone region, the orange box in Fig S12), located in the southwestern U.S. are desert regions with higher soil erodibility than other parts of the domain. It is common in WRF-Chem to tune some of the parameters in the dust emission scheme including the soil erodibility to better match model simulated PM_{10} concentration and AOD with satellite- and ground-based observations (e.g. (Su and Fung, 2015)). This approach has been mainly focusing on the total atmospheric dust load instead of an individual dust event and it is sufficient to capture the general magnitude of dust aerosol patterns. We have adopted this simple approach here to do some dust parameter tuning to improve model simulated surface PM_{10} concentration and AOD with a focus on the overall magnitude.

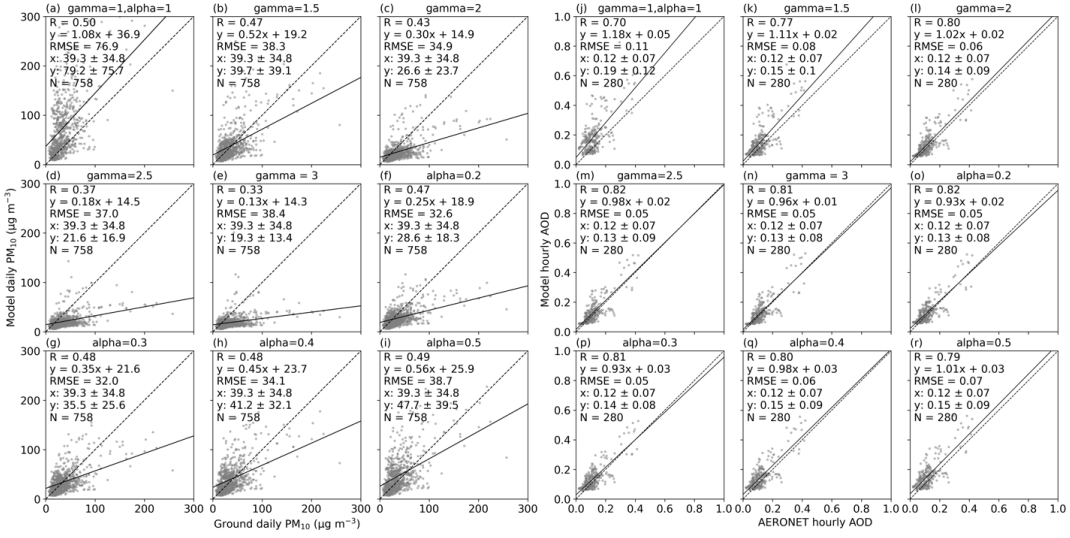

Figure 12. Scatter plot of daily surface PM_{10} concentration and hourly AOD between model (y axis) and ground observation (x axis) over the dust-prone region in USA-LosAngeles for July 2018. (a)–(i) are for surface daily PM_{10} and (j)–(r) are for hourly AOD from two groups of sensitivity simulations: (1) gamma = 1, 1.5, 2, 2.5, 3 while alpha stays as 1; (2) alpha = 0.2, 0.3, 0.4, 0.5 while gamma stays as 1, respectively. Also shown on the scatter plot is the correlation coefficient (*R*), the root-mean-square error (RMSE), the mean ± standard deviation for observed (x) and model-simulated surface PM_{10}/AOD (y), the number of collocated data points (N), the best fit linear regression (the solid black line) and the 1:1 line (the dashed black line).

There are several parameters that can be used to tune dust emissions in the WRF-Chem model. One is the dust_gamma (gamma for short here), which tunes the soil erodibility in an exponential

https://doi.org/10.5194/egusphere-2025-1360
Preprint. Discussion started: 5 May 2025

manner. Soil erodibility serves as an important factor for identifying dust source and estimating dust emission flux in the model. The other one is the dust_alpha (alpha for short here), which linearly tunes the total dust emissions. If we use the default setting (gamma=1, alpha = 1), both model simulated surface daily PM_{10} concentration and hourly AOD overestimate surface measurements of PM_{10} and AOD in the dust-prone region (Fig 12(a) and (j), Fig S13 and S14). Model simulated surface $PM_{2.5}$ concentration also overestimates surface measurements of $PM_{2.5}$ (Fig S13 (a)). We conduct two groups of sensitivity simulations to test the responses of model simulated PM_{10} and AOD to a range of gamma and alpha values, respectively. For the first group test, we set the gamma with 1.5, 2, 2.5 and 3 respectively, while keeping alpha value as 1. For the second group test, we set the alpha with 0.2, 0.3, 0.4, and 0.5 respectively, while keeping gamma value as 1. As gamma increases from 1 to 3 with the constant alpha value of 1, correlation increases for AOD and decreases for surface PM_{10} (Fig 12). MB and RMSE also decreases with increasing gamma value until when gamma value increases to 2.5 for both AOD and PM_{10}. As alpha decreases from 1 to 0.2 with the constant gamma of 1, both MB and RMSE for surface PM_{10} and AOD decrease until alpha value drops to 0.3. The correlation almost stays the same or slightly increases for both PM_{10} and AOD with decreasing alpha value. Therefore, we choose gamma of 1 and alpha of 0.3 as the final configuration to account for the model performance of both PM_{10} and AOD.

Here, we use one month of data to tune the dust emissions by focusing on the magnitude of the total dust load. It is challenging to fine tune each individual dust event and acquire consistent results. The work of Hyde et al. (2018) simulated nine dust storms in south-central Arizona with WRF-Chem using the GOCART AFWA dust emission scheme and the model unevenly reproduced the dust-storm events with some cases overestimating surface PM_{10} and some cases underestimating surface PM_{10}. Our evaluation of AOD with AERONET observation is rather limited spatially as we only have one AERONET site for the dust-prone region. We also conduct the same set of sensitivity simulations for July 2019 (results not shown here) and the sensitivities to the tuned parameters are comparable to the results of 2018 in general, which further confirms the validity of the simple approach we have used here. Additionally, more recent work have incorporated the albedo-based drag partition (Chappell and Webb, 2016) from satellite data into the GOCART AFWA dust emission scheme to better represent the impacts of roughness features from vegetation and non-vegetation such as soil and rocks and demonstrated improved model performance in capturing individual dust event over the Southwestern U.S. (Legrand et al., 2023; Dhital et al., 2024). It is beyond the scope of this work to implement this method, but future work could explore the use of this advanced method and focus on longer periods of model simulation to further evaluate model performances.

4.3.2 Case study – USA-Atlanta

As described in Sect 3, for the standard PTA nested domain setup, we have chosen to turn off the cumulus parameterization in the inner domain (D2) with the spatial resolution of 4 km and let the

https://doi.org/10.5194/egusphere-2025-1360
Preprint. Discussion started: 5 May 2025

model rely on the microphysics scheme to explicitly resolve the convection. Southeastern U.S. including the PTA-Atlanta (Fig 1(d)) target area experiences pulse-type summer convective precipitation due to the interplay of land-sea breezes, outflow boundaries and complex terrain etc. (Case et al., 2011). Here, we focus on June 2022 over PTA-Atlanta to demonstrate the impacts of different setups of microphysics and cumulus schemes on model simulated precipitation and subsequent surface $PM_{2.5}$ concentration. We perform six UI-WRF-Chem sensitivity simulations with different setups of microphysics and cumulus schemes while keeping other schemes the same: (1) mp2cu5: Both domain 1 and domain 2 have the Lin microphysics scheme on. Domain 1 and domain 2 have the G3D cumulus scheme on and off, respectively; (2) mp2cu5bothon: same as (1) except that both domain and 1 and domain 2 have the G3D cumulus scheme on; (3) mp2cu3bothon: same as (2) except that both domain 1 and domain 2 have the GF cumulus scheme on; (4) mp10cu5; (5) mp10cu5bothon; and (6) mp10cu3bothon. (4)–(6) are the same as (1)–(3) except that both domain 1 and domain 2 have the Morrison microphysics scheme on. Here, the difference between (1) and (2) illustrates the impacts of turning on/off the cumulus scheme at the 4 km resolution. The difference between (1), (2) and (1), (3) evaluates the impacts of using a traditional cumulus scheme vs. a scale-aware cumulus scheme. Corresponding difference between (1)–(3) and (4)–(6) represents the impacts of the microphysics scheme.

We first focus on the evaluation of daily precipitation. Although, hourly precipitation rate can be important to tell the intensity of the precipitation event, verification of the hourly precipitation can raise double-penalty issues at the finer resolution (Rossa et al., 2008; Gilleland et al., 2009), where a slight shift in the prediction of the timing or location of the precipitation event compared with the ground truth could result in the verification penalties in both space-time. Here, we accumulate the hourly precipitation into daily precipitation to help offset the errors associated with the timing of the event. Figure S15 shows the monthly averaged daily precipitation from UI-WRF-Chem model sensitivity simulations (1)–(6) with surface observations. In general, all the sensitivity runs overestimate the precipitation. Turning on the cumulus scheme in domain 2 when using the traditional G3D scheme results in larger bias compared to the results of turning the G3D scheme off. The work of Zhang et al. (2021) also found that the WRF model had better prediction of precipitation in the central Great Plains in the U.S. when turning off the G3D cumulus scheme with the spatial resolution of 4 km, compared to the sensitivity run of turning on the G3D cumulus scheme. Turning off the cumulus scheme in domain 2 when using the G3D scheme is comparable to the results of the simulation using the scale-aware GF cumulus scheme.

We then focus on the impacts on surface $PM_{2.5}$ concentration. Figure S16 shows the spatial map of surface $PM_{2.5}$ concentration for June 2022 and Fig 13 compares model simulated daily $PM_{2.5}$ concentration with ground observation. Both sensitivity simulations (2) and (4) with the G3D scheme on for the inner domain (D2) simulate higher precipitation than other simulations, which leads to lower surface $PM_{2.5}$ concentration (Fig S16(b) and (e)). Overall, the surface $PM_{2.5}$ concentration from sensitivity simulations (2) and (4) have the lowest correlation (0.34 and 0.49)

https://doi.org/10.5194/egusphere-2025-1360
Preprint. Discussion started: 5 May 2025

compared to other simulation (0.52–0.61) (Fig 13). They also have higher MB (–5.1 μg m^{-3} and –5.9 μg m^{-3}) compared with other simulations (–4.7 to –3.2 μg m^{-3}) (Fig 13). Sensitivity simulations over CHN-Beijing also show similar results related to surface $PM_{2.5}$ concentration when contrasting the sensitivity simulation with or without the G3D cumulus on for the inner domain (not shown here). This validates our choice of turning the cumulus scheme off for the inner domain (D2) when using the traditional cumulus scheme such as G3D. Surface $PM_{2.5}$ concentration from the sensitivity simulations, which turn off the G3D cumulus scheme ((1) and (4)) is comparable to or even better than the results from the sensitivity simulations (3) and (6) which turn on the scale-aware cumulus scheme GF.

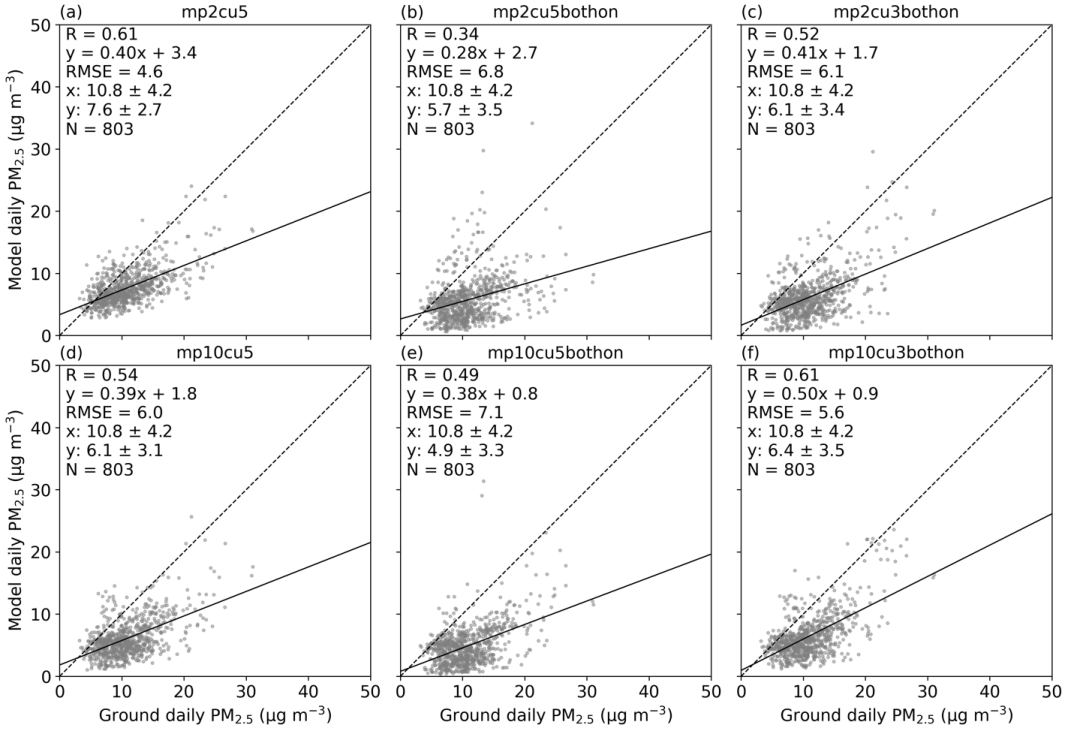

Figure 13. Scatter plot of daily surface $PM_{2.5}$ concentration between model (y axis) and ground observation (x axis) over the inner domain (D2) of USA-Atlanta for June 2022. (a)–(f) are the UI-WRF-Chem sensitivity simulations with different setups of microphysics and cumulus schemes. (a)–(c) all have the Lin microphysics scheme on for domain 1. (a) has the Lin microphysics scheme on for domain 2 and no cumulus scheme is used for domain 2. (b) is the same as (a) except that the G3D cumulus scheme is turned on for domain 2. (c) is same as (b) except that the GF cumulus scheme is used for domain 2. (d)–(f) are the same as (a)–(c) except that the Morrison microphysics scheme is used for both domain 1 and domain 2. Also shown on the scatter plot is the correlation coefficient (*R*), the root-mean-square error (RMSE), the mean ± standard deviation for observed (x) and model-simulated surface $PM_{2.5}$ (y), the number of collocated data points (N), the best fit linear regression (the solid black line) and the 1:1 line (the dashed black line).

https://doi.org/10.5194/egusphere-2025-1360
Preprint. Discussion started: 5 May 2025

There are some uncertainties in this case study. First, our evaluation is limited in time. A longer dataset would be more helpful to reveal model performances in other seasons too (Jeworrek et al., 2021). Also, we have only considered a limited number of model configurations. Previous work have shown that the prediction of precipitation is also sensitive to other schemes in the model such as the PBL scheme (Klein et al., 2015; Argüeso et al., 2011). Most previous work have focused on the impacts of microphysics and cumulus scheme on precipitation and less have focused on the coupling with the aerosol fields. The process of handling aerosol-cloud interactions would be another source of uncertainty here. Lastly, deficiencies in MERRA-2 boundary conditions could also introduce uncertainties or biases in the WRF-Chem simulation (Zhang et al., 2021).

5. Conclusion and discussion

We have developed the Unified Inputs (of initial and boundary conditions) for WRF-Chem (UI-WRF-Chem) modeling framework, based on the standard WRF-Chem model to support the MAIA satellite mission, which aims to study how different types of PM air pollution affect human health. The UI-WRF-Chem outputs will be integrated together with satellite and ground observations data to generate surface total PM and speciated PM maps. We have made the following major updates in the UI-WRF-Chem modeling framework: (1) using NASA GEOS data including GEOS FP and MERRA-2 data to provide both meteorological and chemical initial and boundary conditions to drive WRF-Chem simulations at a finer spatial resolution for both forecasting and reanalysis modes; (2) developing the WEPS stand-alone module to process both global and regional anthropogenic emissions as well as fire emissions; (3) updating land surface properties (land cover type, LAI, GVF and albedo) with MODIS land products in a timely fashion; (4) using a global or regional land data assimilation system (GLDAS or NLDAS) to constrain soil properties (soil temperature and moisture etc.); and (5) developing a new soil NO_x emission scheme - BDISNP.

In this work, we focus on four target areas to demonstrate the application of the UI-WRF-Chem modeling framework: CHN-Beijing, ITA-Rome, USA-LosAngeles and USA-Atlanta. Each target area is set up with 2 nested domains with a 12 km and 4 km spatial resolution for the outer domain (D1) and inner domain (D2), respectively. First, we conduct a suite of sensitivity simulations over each target area to select the optimal combination of physics schemes used in the model. We have chosen to turn off the cumulus scheme for the inner domain (D2) since we are using the traditional G3D cumulus scheme, which is not a scale-aware scheme. We investigate the impacts of cumulus scheme and microphysics scheme on model performance over the USA-Atlanta target area for June 2022. Our case study shows that turning on the G3D cumulus scheme in the inner domain (D2) will produce higher precipitation than the sensitivity simulation with the G3D scheme off, which in turn leads to lower surface $PM_{2.5}$ concentration. Compared with surface observations of precipitation and $PM_{2.5}$ concentration, the sensitivity simulation with the G3D scheme off shows better performance than keeping it on. Due to the problem with the scale-aware GF cumulus

https://doi.org/10.5194/egusphere-2025-1360
Preprint. Discussion started: 5 May 2025

scheme in the model (not coupled to the chemistry), we are not able to fully investigate the use of a scale-aware scheme on model performance in the current work. Future work will explore the use of this scale-aware scheme with longer periods of simulation and in other target areas.

Both CHN-Beijing and ITA-Rome target areas are affected by dust long-range transport. We select two dust intrusion events that impacted these two target areas. A dust storm originated from the Taklamakan and Gobi Deserts around 24 March 2018 and moved downwind to CHN-Beijing from 27 to 28 March 2018. For ITA-Rome, we focus on June 2023 where Saharan dust transported to the target area. For both target areas, we conduct UI-WRF-Chem sensitivity simulations with different chemical boundary conditions being considered using MERRA-2 data: no chemical species considered; including dust and other aerosols. Here, we also develop a method to constrain the dust concentration for each size bin in the MERRA-2 data using AERONET data. We compare the dust PSD from MERRA-2 data with AERONET observations to better distribute the dust concentration in different size bins in the MERRA-2 chemical boundary conditions, based on long-term datasets. Our results show that including the dust and other aerosols in the boundary improve model simulated surface PM concentration and AOD during dust intrusion events for both target areas, compared to the model run without using MERRA-2 chemical boundary conditions. Using the constrained dust concentration in the MERRA-2 data further improve model performance. This method helps reduce the computational cost when long-range transport or regional transport affects a target area. Otherwise, we would need to add a third nested domain with expanded domain size to cover the pollution sources such as the dust source region.

Updating land surface properties (land cover type, LAI, GVF and surface albedo) with MODIS land data in a timely fashion improves model simulated TSK compared with MODIS LST, which is demonstrated over the CHN-Beijing target area for July 2018. This could help better capture the UHI phenomenon, which leads to better simulation of processes that are important for surface PM simulation. For other PTAs who have experienced rapid urbanization, updating land cover type and other land surface properties with timely MODIS land data can be important. We also recognize that we have not investigated the use of an urban canopy model to simulate the UHI effect in the UI-WRF-Chem framework. The newly updated BDISNP soil NO_x emission scheme improves the simulation of NO_2 which subsequently affects surface nitrate. Evaluated against TROPOMI NO_2 VCD, the updated BDISNP soil NO_x emission scheme increases NO_2 VCD, mainly over croplands in CHN-Beijing target area than the simulation using the default MEGAN soil NO_x emission scheme, which is mainly due to the application of fertilizer use. Since the ground observations of surface NO_2, O_3, and $PM_{2.5}$ concentration are mostly located in the urban areas, we acknowledge that our current work is limited, and efforts will need to further evaluate the impacts of this updated BDISNP scheme in the rural areas. Nevertheless, the launch of the GEMS and the Tropospheric Emissions: Monitoring of Pollution (TEMPO) (Zoogman et al., 2017) satellites will provide good opportunities to further refine the BDISNP scheme. The synergy between MAIA and GEMS/TEMPO will also provide opportunities to evaluate both gas and aerosol composition simultaneously.

https://doi.org/10.5194/egusphere-2025-1360
Preprint. Discussion started: 5 May 2025

We also perform a case study over the USA-LosAngeles target area, where we tune dust emissions inside the target area. Southwestern U.S., covering part of the USA-LosAngeles target area are desert areas, which experience dust outbreaks. If we use the default dust emission scheme, the model simulated surface PM and AOD overestimate ground observations. We conduct sensitivity tests to fine tune the parameters in the dust emission scheme as commonly done in the literature to find the optimal parameter. As we have been conducting model performance evaluation, we can do some fine-tuning over each target area to investigate the problem specific to that target area. The case study over USA-LosAngeles gives an example of the fine-tuning work we are doing. As part of the MAIA satellite mission, UI-WRF-Chem model outputs will also be further evaluated by the surface measurements of aerosol composition data that will be collected in various PTAs through the Surface Particulate Matter Network (SPARTAN) (Snider et al., 2015) and other existing networks in the target areas. Selection of physics schemes for other PTAs and other model evaluation results will be documented in a technical guide to complement this paper.

Code and data availability

The codes used in this work are available at: https://zenodo.org/records/15074108 (Zhang, 2025a). WRF-Chem is an open-access model, which is available at: https://github.com/wrf-model/WRF/releases. The WRF-Chem preprocessor tools including mozbc, bio_emiss, anthro_emiss and EPA_ANTHRO_EMIS are available at: https://www2.acom.ucar.edu/wrf-chem/wrf-chem-tools-community. Input files for bio_emiss and U.S. EPA NEI 2017 data can also be acquired from this website. EDGAR-HTAP global anthropogenic emission data are available at: https://edgar.jrc.ec.europa.eu/dataset_htap_v3. MEIC anthropogenic emission data for China are available at: http://meicmodel.org.cn/?page_id=1772&lang=en. MODIS and VIIRS data are available at: https://ladsweb.modaps.eosdis.nasa.gov/; CALIOP data are downloaded from https://asdc.larc.nasa.gov/project/CALIPSO; MERRA-2, GLDAS, NLDAS and TROPOIMI and GPM data can be acquired from https://disc.gsfc.nasa.gov/. Both ground observations of meteorology and PM data for Beijing are available at: https://quotsoft.net/air/. Ground observations of meteorology and PM data for Los Angeles as well as PM data for Atlanta are from https://aqs.epa.gov/aqsweb/airdata/download_files.html. Ground observations of meteorology data for Rome and Atlanta are from https://www.ncei.noaa.gov/pub/data/noaa/isd-lite/. Ground observations of PM data for Rome are available from https://search.earthdata.nasa.gov/search (use key words MAIA PM data). AERONET data can be downloaded at: https://aeronet.gsfc.nasa.gov/. Other datasets that are used and created in this work are available at: https://zenodo.org/records/15239059 (Zhang, 2025b).

https://doi.org/10.5194/egusphere-2025-1360
Preprint. Discussion started: 5 May 2025

Author contributions

HZ and JW conceived and designed the study. HZ performed all the simulations except for the Los Angeles case, conducted data analysis and wrote the initial manuscript draft. CG and JW constructed the UI-WRF-Chem modeling framework at the initial stage. HZ and NJ later served as the main developers for the UI-WRF-Chem modeling framework, under the guidance of JW. HZ manages the ongoing code updates. MZ developed the method of using AERONET climatology data to constrain the MERRA-2 dust concentration for each size bin when updating chemical boundary conditions and contributed to the selection of physics schemes used for model configuration. LCG supported the development of Linux scripts, data acquisition and Python code development. TS developed the BDISNP soil NO_x emission scheme with the assistance of HZ and NJ and YiW improved the soil temperature response function within the scheme. YaW developed the modules to update land surface properties using MODIS data with support from HZ and NJ. CL updated the NEI 2017 and EDGAR-HTAP v3 emission inventories in the WEPS module with guidance from HZ. WD conducted the simulation for Los Angeles and ZX contributed to the simulation for Atlanta. WD, ZX and LC contributed to updates of land surface properties. HZ and SV collaborated on verifying the implementation of UI-WRF-Chem modeling framework and SV contributed to the design of the framework for operational use. JLM, SEG and DJD provided feedback on the implementation of the UI-WRF-Chem modeling framework in support of the MAIA satellite mission. SH assisted with the use of surface observation of PM in Italy. PRC and AMDS provided support and guidance on the use of GEOS data. All authors contributed to the manuscript revision.

Competing interests

The authors declare that they have no conflict of interest.

Acknowledgements

We sincerely thank NASA JPL for funding this research. We acknowledge the public availability of the various satellite datasets used here from NASA's different Distributed Active Archive Centers (DAACs): MODIS and VIIRS data from Level 1 and Atmosphere Archive and Distribution System (LAADS DAAC); the CALIOP data from Atmospheric Science Data Center (ASDC) at NASA's Langley Research Center; MERRA-2, GLDAS, NLDAS, TROPOMI and GPM data from the Goddard Earth Sciences Data and Information Service Center (GES DISC). We are grateful for the ground observations of meteorology variables (e.g t2), provided by the Meteorological Information Comprehensive Analysis and Process System (MICAPS) in China, U.S. EPA and National Centers for Environmental Information (NCEI) Integrated Surface Database (ISD). We are thankful for the availability of ground observations of surface $PM_{2.5}$ and PM_{10} concentration from environmental monitoring stations managed by the Ministry of

https://doi.org/10.5194/egusphere-2025-1360
Preprint. Discussion started: 5 May 2025

Environmental Protection in China, U.S. EPA, and ARPA Lazio and ARPAE Emilia Romagna in Italy. We appreciate the AERONET networks for making their data publicly available and are grateful for the site PIs and data managers of the networks. We acknowledge the use of the WPS component in the NU-WRF system, which is available at: https://nuwrf.gsfc.nasa.gov/. We also acknowledge the use of the various WRF-Chem preprocessor tools (mozbc, bio_emiss, anthro_emiss and EPA_ANTHRO_EMIS), provided by the Atmospheric Chemistry Observations and Modeling Lab (ACOM) of National Center for Atmospheric Research (NCAR). We are also grateful for the anthropogenic emission inventories available to the public: EDGAR-HTAP global dataset provided by the European Commission, U.S. EPA NEI dataset by U.S. EPA and MEIC emission dataset for China provided by Tsinghua University. We thank Dr. Edward Hyer from the Naval Research Laboratory (NRL) for providing FLAMBE emission inventories. We also thank the Argon High-performance Computing (HPC) system at the University of Iowa for the support.

https://doi.org/10.5194/egusphere-2025-1360
Preprint. Discussion started: 5 May 2025

References

Ackermann, I. J., Hass, H., Memmesheimer, M., Ebel, A., Binkowski, F. S., and Shankar, U.: Modal aerosol dynamics model for Europe: Development and first applications, Atmospheric environment, 32, 2981-2999, 1998.

Adams-Selin, R. D., van den Heever, S. C., and Johnson, R. H.: Sensitivity of Bow-Echo Simulation to Microphysical Parameterizations, Weather and Forecasting, 28, 1188-1209, https://doi.org/10.1175/WAF-D-12-00108.1, 2013.

Aegerter, C., Wang, J., Ge, C., Irmak, S., Oglesby, R., Wardlow, B., Yang, H., You, J., and Shulski, M.: Mesoscale Modeling of the Meteorological Impacts of Irrigation during the 2012 Central Plains Drought, Journal of Applied Meteorology and Climatology, 56, 1259-1283, 2017.

Argüeso, D., Hidalgo-Muñoz, J. M., Gámiz-Fortis, S. R., Esteban-Parra, M. J., Dudhia, J., and Castro-Díez, Y.: Evaluation of WRF parameterizations for climate studies over southern Spain using a multistep regionalization, Journal of Climate, 24, 5633-5651, 2011.

Barnaba, F., Alvan Romero, N., Bolignano, A., Basart, S., Renzi, M., and Stafoggia, M.: Multiannual assessment of the desert dust impact on air quality in Italy combining PM10 data with physics-based and geostatistical models, Environment International, 163, 107204, https://doi.org/10.1016/j.envint.2022.107204, 2022.

Barnard, J. C., Fast, J. D., Paredes-Miranda, G., Arnott, W., and Laskin, A.: Evaluation of the WRF-Chem" Aerosol Chemical to Aerosol Optical Properties" Module using data from the MILAGRO campaign, Atmospheric Chemistry and Physics, 10, 7325-7340, 2010.

Binkowski, F. S. and Shankar, U.: The Regional Particulate Matter Model: 1. Model description and preliminary results, Journal of Geophysical Research: Atmospheres, 100, 26191-26209, 10.1029/95jd02093, 1995.

Brisson, E., Demuzere, M., and Van Lipzig, N.: Modelling strategies for performing convection-permitting climate simulations, Meteorologische Zeitschrift, 25, 149-163, 2015.

Broxton, P. D., Zeng, X., Sulla-Menashe, D., and Troch, P. A.: A Global Land Cover Climatology Using MODIS Data, Journal of Applied Meteorology and Climatology, 53, 1593-1605, 10.1175/JAMC-D-13-0270.1, 2014.

Case, J. L., Kumar, S. V., Srikishen, J., and Jedlovec, G. J.: Improving Numerical Weather Predictions of Summertime Precipitation over the Southeastern United States through a High-Resolution Initialization of the Surface State, Weather and Forecasting, 26, 785-807, https://doi.org/10.1175/2011WAF2222455.1, 2011.

Chappell, A. and Webb, N. P.: Using albedo to reform wind erosion modelling, mapping and monitoring, Aeolian Research, 23, 63-78, https://doi.org/10.1016/j.aeolia.2016.09.006, 2016.

Chen, F. and Dudhia, J.: Coupling an advanced land surface–hydrology model with the Penn State–NCAR MM5 modeling system. Part I: Model implementation and sensitivity, Monthly weather review, 129, 569-585, 2001.

Chen, F., Mitchell, K., Schaake, J., Xue, Y., Pan, H. L., Koren, V., Duan, Q. Y., Ek, M., and Betts, A.: Modeling of land surface evaporation by four schemes and comparison with FIFE observations, Journal of Geophysical Research: Atmospheres, 101, 7251-7268, 1996.

Chen, S.-H. and Sun, W.-Y.: A one-dimensional time dependent cloud model, Journal of the Meteorological Society of Japan. Ser. II, 80, 99-118, 2002.

Chin, M., Ginoux, P., Kinne, S., Torres, O., Holben, B. N., Duncan, B. N., Martin, R. V., Logan, J. A., Higurashi, A., and Nakajima, T.: Tropospheric aerosol optical thickness from the GOCART model and comparisons with satellite and Sun photometer measurements, Journal of the atmospheric sciences, 59, 461-483, 2002.

Chou, M.-D., Suarez, M. J., Ho, C.-H., Yan, M. M., and Lee, K.-T.: Parameterizations for cloud overlapping and shortwave single-scattering properties for use in general circulation and cloud ensemble models, Journal of climate, 11, 202-214, 1998.

Chutia, L., Wang, J., Zhang, H., Chen, X., Castro Garcia, L., and Janechek, N.: Elucidating the impacts of aerosol radiative effects for mitigating surface O3 and PM2.5 in Delhi, India during crop residue burning period, Atmospheric Environment, 339, 120890, https://doi.org/10.1016/j.atmosenv.2024.120890, 2024.

Clark, A. J., Gallus, W. A., Xue, M., and Kong, F.: A comparison of precipitation forecast skill between small convection-allowing and large convection-parameterizing ensembles, Weather and forecasting, 24, 1121-1140, 2009.

Clinton, N. and Gong, P.: MODIS detected surface urban heat islands and sinks: Global locations and controls, Remote Sensing of Environment, 134, 294-304, 2013.

Cohen, A. J., Brauer, M., Burnett, R., Anderson, H. R., Frostad, J., Estep, K., Balakrishnan, K., Brunekreef, B., Dandona, L., and Dandona, R.: Estimates and 25-year trends of the global burden of disease attributable to ambient air pollution: an analysis of data from the Global Burden of Diseases Study 2015, The Lancet, 389, 1907-1918, 2017.

Colarco, P., da Silva, A., Chin, M., and Diehl, T.: Online simulations of global aerosol distributions in the NASA GEOS-4 model and comparisons to satellite and ground-based aerosol optical depth, Journal of Geophysical Research: Atmospheres, 115, https://doi.org/10.1029/2009JD012820, 2010.

https://doi.org/10.5194/egusphere-2025-1360
Preprint. Discussion started: 5 May 2025

Crippa, M., Solazzo, E., Huang, G., Guizzardi, D., Koffi, E., Muntean, M., Schieberle, C., Friedrich, R., and Janssens-Maenhout, G.: High resolution temporal profiles in the Emissions Database for Global Atmospheric Research, Scientific Data, 7, 121, 10.1038/s41597-020-0462-2, 2020.

Crippa, M., Guizzardi, D., Butler, T., Keating, T., Wu, R., Kaminski, J., Kuenen, J., Kurokawa, J., Chatani, S., Morikawa, T., Pouliot, G., Racine, J., Moran, M. D., Klimont, Z., Manseau, P. M., Mashayekhi, R., Henderson, B. H., Smith, S. J., Suchyta, H., Muntean, M., Solazzo, E., Banja, M., Schaaf, E., Pagani, F., Woo, J. H., Kim, J., Monforti-Ferrario, F., Pisoni, E., Zhang, J., Niemi, D., Sassi, M., Ansari, T., and Foley, K.: The HTAP_v3 emission mosaic: merging regional and global monthly emissions (2000–2018) to support air quality modelling and policies, Earth Syst. Sci. Data, 15, 2667-2694, 10.5194/essd-15-2667-2023, 2023.

Darmenov, A. and da Silva, A.: The quick fire emissions dataset (QFED):Documentation of versions 2.1, 2.2 and 2.4, NASA/TM–2015–104606, 2015.

de Rosnay, P., Balsamo, G., Albergel, C., Muñoz-Sabater, J., and Isaksen, L.: Initialisation of land surface variables for numerical weather prediction, Surveys in Geophysics, 35, 607-621, 2014.

Dhital, S., Webb, N. P., Chappell, A., Kaplan, M. L., Nauman, T. W., Tyree, G., Duniway, M. C., Edwards, B., LeGrand, S. L., Letcher, T. W., McKenzie Skiles, S., Naple, P., Chaney, N. W., and Cai, J.: Synoptic Analysis and WRF-Chem Model Simulation of Dust Events in the Southwestern United States, Journal of Geophysical Research: Atmospheres, 129, e2023JD040650, https://doi.org/10.1029/2023JD040650, 2024.

Diao, M., Holloway, T., Choi, S., O'Neill, S. M., Al-Hamdan, M. Z., Van Donkelaar, A., Martin, R. V., Jin, X., Fiore, A. M., Henze, D. K., Lacey, F., Kinney, P. L., Freedman, F., Larkin, N. K., Zou, Y., Kelly, J. T., and Vaidyanathan, A.: Methods, availability, and applications of PM2.5 exposure estimates derived from ground measurements, satellite, and atmospheric models, Journal of the Air & Waste Management Association, 69, 1391-1414, 10.1080/10962247.2019.1668498, 2019.

Dillon, M. E., Collini, E. A., and Ferreira, L. J.: Sensitivity of WRF short-term forecasts to different soil moisture initializations from the GLDAS database over South America in March 2009, Atmospheric Research, 167, 196-207, https://doi.org/10.1016/j.atmosres.2015.07.022, 2016.

Diner, D. J., Beckert, J. C., Reilly, T. H., Bruegge, C. J., Conel, J. E., Kahn, R. A., Martonchik, J. V., Ackerman, T. P., Davies, R., and Gerstl, S. A.: Multi-angle Imaging SpectroRadiometer (MISR) instrument description and experiment overview, IEEE Transactions on Geoscience and Remote Sensing, 36, 1072-1087, 1998.

Diner, D. J., Boland, S. W., Brauer, M., Bruegge, C., Burke, K. A., Chipman, R., Di Girolamo, L., Garay, M. J., Hasheminassab, S., and Hyer, E.: Advances in multiangle satellite remote sensing of speciated airborne particulate matter and association with adverse health effects: from MISR to MAIA, Journal of Applied Remote Sensing, 12, 042603, 2018.

Done, J., Davis, C. A., and Weisman, M.: The next generation of NWP: explicit forecasts of convection using the weather research and forecasting (WRF) model, Atmospheric Science Letters, 5, 110-117, https://doi.org/10.1002/asl.72, 2004.

Du, Q., Zhao, C., Zhang, M., Dong, X., Chen, Y., Liu, Z., Hu, Z., Zhang, Q., Li, Y., Yuan, R., and Miao, S.: Modeling diurnal variation of surface PM2.5 concentrations over East China with WRF-Chem: impacts from boundary-layer mixing and anthropogenic emission, Atmos. Chem. Phys., 20, 2839-2863, 10.5194/acp-20-2839-2020, 2020.

Dudhia, J.: A history of mesoscale model development, Asia-Pacific Journal of Atmospheric Sciences, 50, 121-131, 2014.

Emmons, L. K., Schwantes, R. H., Orlando, J. J., Tyndall, G., Kinnison, D., Lamarque, J.-F., Marsh, D., Mills, M. J., Tilmes, S., Bardeen, C., Buchholz, R. R., Conley, A., Gettelman, A., Garcia, R., Simpson, I., Blake, D. R., Meinardi, S., and Pétron, G.: The Chemistry Mechanism in the Community Earth System Model Version 2 (CESM2), Journal of Advances in Modeling Earth Systems, 12, e2019MS001882, https://doi.org/10.1029/2019MS001882, 2020.

Fast, J. D., Gustafson Jr, W. I., Easter, R. C., Zaveri, R. A., Barnard, J. C., Chapman, E. G., Grell, G. A., and Peckham, S. E.: Evolution of ozone, particulates, and aerosol direct radiative forcing in the vicinity of Houston using a fully coupled meteorology-chemistry-aerosol model, Journal of Geophysical Research: Atmospheres, 111, 2006.

Forouzanfar, M. H. and Afshin, A. and Alexander, L. T. and Anderson, H. R. and Bhutta, Z. A. and Biryukov, S. and Brauer, M. and Burnett, R. and Cercy, K. and Charlson, F. J. and Cohen, A. J. and Dandona, L. and Estep, K. and Ferrari, A. J. and Frostad, J. J. and Fullman, N. and Gething, P. W. and Godwin, W. W. and Griswold, M. and Hay, S. I. and Kinfu, Y. and Kyu, H. H. and Larson, H. J. and Liang, X. and Lim, S. S. and Liu, P. Y. and Lopez, A. D. and Lozano, R. and Marczak, L. and Mensah, G. A. and Mokdad, A. H. and Moradi-Lakeh, M. and Naghavi, M. and Neal, B. and Reitsma, M. B. and Roth, G. A. and Salomon, J. A. and Sur, P. J. and Vos, T. and Wagner, J. A. and Wang, H. and Zhao, Y. and Zhou, M. and Aasvang, G. M. and Abajobir, A. A. and Abate, K. H. and Abbafati, C. and Abbas, K. M. and Abd-Allah, F. and Abdulle, A. M. and Abera, S. F. and Abraham, B. and Abu-Raddad, L. J. and Abyu, G. Y. and Adebiyi, A. O. and Adedeji, I. A. and Ademi, Z. and Adou, A. K. and Adsuar, J. C. and Agardh, E. E. and Agarwal, A. and Agrawal, A. and Kiadaliri, A. A. and Ajala, O. N. and Akinyemiju, T. F. and Al-Aly, Z. and Alam, K. and Alam, N. K. M. and Aldhahri, S. F. and Aldridge, R. W. and Alemu, Z. A. and Ali, R. and Alkerwi, A. a. and Alla, F. and Allebeck, P. and Alsharif, U. and Altirkawi, K. A. and Martin, E. A. and Alvis-Guzman, N. and Amare, A. T. and Amberbir, A. and Amegah, A. K. and Amini, H. and Ammar, W. and Amrock, S. M. and Andersen, H. H. and Anderson, B. O. and Antonio, C.

https://doi.org/10.5194/egusphere-2025-1360
Preprint. Discussion started: 5 May 2025

A. T. and Anwari, P. and Ärnlöv, J. and Artaman, A. and Asayesh, H. and Asghar, R. J. and Assadi, R. and Atique, S. and Avokpaho, E. F. G. A. and Awasthi, A. and Quintanilla, B. P. A. and Azzopardi, P. and Bacha, U. and Badawi, A. and Bahit, M. C. and Balakrishnan, K. and Barac, A. and Barber, R. M. and Barker-Collo, S. L. and Bärnighausen, T. and Barquera, S. and Barregard, L. and Barrero, L. H. and Basu, S. and Batis, C. and Bazargan-Hejazi, S. and Beardsley, J. and Bedi, N. and Beghi, E. and Bell, B. and Bell, M. L. and Bello, A. K. and Bennett, D. A. and Bensenor, I. M. and Berhane, A. and Bernabé, E. and Betsu, B. D. and Beyene, A. S. and Bhala, N. and Bhansali, A. and Bhatt, S. and Biadgilign, S. and Bikbov, B. and Bisanzio, D. and Bjertness, E. and Blore, J. D. and Borschmann, R. and Boufous, S. and Bourne, R. R. A. and Brainin, M. and Brazinova, A. and Breitborde, N. J. K. and Brenner, H. and Broday, D. M. and Brugha, T. S. and Brunekreef, B. and Butt, Z. A. and Cahill, L. E. and Calabria, B. and Campos-Nonato, I. R. and Cárdenas, R. and Carpenter, D. O. and Carrero, J. J. and Casey, D. C. and Castañeda-Orjuela, C. A. and Rivas, J. C. and Castro, R. E. and Catalá-López, F. and Chang, J.-C. and Chiang, P. P.-C. and Chibalabala, M. and Chimed-Ochir, O. and Chisumpa, V. H. and Chitheer, A. A. and Choi, J.-Y. J. and Christensen, H. and Christopher, D. J. and Ciobanu, L. G. and Coates, M. M. and Colquhoun, S. M. and Manzano, A. G. C. and Cooper, L. T. and Cooperrider, K. and Cornaby, L. and Cortinovis, M. and Crump, J. A. and Cuevas-Nasu, L. and Damasceno, A. and Dandona, R. and Darby, S. C. and Dargan, P. I. and das Neves, J. and Davis, A. C. and Davletov, K. and de Castro, E. F. and De la Cruz-Góngora, V. and De Leo, D. and Degenhardt, L. and Del Gobbo, L. C. and del Pozo-Cruz, B. and Dellavalle, R. P. and Deribew, A. and Jarlais, D. C. D. and Dharmaratne, S. D. and Dhillon, P. K. and Diaz-Torné, C. and Dicker, D. and Ding, E. L. and Dorsey, E. R. and Doyle, K. E. and Driscoll, T. R. and Duan, L. and Dubey, M. and Duncan, B. B. and Elyazar, I. and Endries, A. Y. and Ermakov, S. P. and Erskine, H. E. and Eshrati, B. and Esteghamati, A. and Fahimi, S. and Faraon, E. J. A. and Farid, T. A. and Farinha, C. S. e. S. and Faro, A. and Farvid, M. S. and Farzadfar, F. and Feigin, V. L. and Fereshtehnejad, S.-M. and Fernandes, J. G. and Fischer, F. and Fitchett, J. R. A. and Fleming, T. and Foigt, N. and Foreman, K. and Fowkes, F. G. R. and Franklin, R. C. and Fürst, T. and Futran, N. D. and Gakidou, E. and Garcia-Basteiro, A. L. and Gebrehiwot, T. T. and Gebremedhin, A. T. and Geleijnse, J. M. and Gessner, B. D. and Giref, A. Z. and Giroud, M. and Gishu, M. D. and Giussani, G. and Goenka, S. and Gomez-Cabrera, M. C. and Gomez-Dantes, H. and Gona, P. and Goodridge, A. and Gopalani, S. V. and Gotay, C. C. and Goto, A. and Gouda, H. N. and Gugnani, H. C. and Guillemin, F. and Guo, Y. and Gupta, R. and Gupta, R. and Gutiérrez, R. A. and Haagsma, J. A. and Hafezi-Nejad, N. and Haile, D. and Hailu, G. B. and Halasa, Y. A. and Hamadeh, R. R. and Hamidi, S. and Handal, A. J. and Hankey, G. J. and Hao, Y. and Harb, H. L. and Harikrishnan, S. and Haro, J. M. and Hassanvand, M. S. and Hassen, T. A. and Havmoeller, R. and Heredia-Pi, I. B. and Hernández-Llanes, N. F. and Heydarpour, P. and Hoek, H. W. and Hoffman, H. J. and Horino, M. and Horita, N. and Hosgood, H. D. and Hoy, D. G. and Hsairi, M. and Htet, A. S. and Hu, G. and Huang, J. J. and Husseini, A. and Hutchings, S. J. and Huybrechts, I. and Iburg, K. M. and Idrisov, B. T. and Ileanu, B. V. and Inoue, M. and Jacobs, T. A. and Jacobsen, K. H. and Jahanmehr, N. and Jakovljevic, M. B. and Jansen, H. A. F. M. and Jassal, S. K. and Javanbakht, M. and Jayaraman, S. P. and Jayatilleke, A. U. and Jee, S. H. and Jeemon, P. and Jha, V. and Jiang, Y. and Jibat, T. and Jin, Y. and Johnson, C. O. and Jonas, J. B. and Kabir, Z. and Kalkonde, Y. and Kamal, R. and Kan, H. and Karch, A. and Karema, C. K. and Karimkhani, C. and Kasaeian, A. and Kaul, A. and Kawakami, N. and Kazi, D. S. and Keiyoro, P. N. and Kemmer, L. and Kemp, A. H. and Kengne, A. P. and Keren, A. and Kesavachandran, C. N. and Khader, Y. S. and Khan, A. R. and Khan, E. A. and Khan, G. and Khang, Y.-H. and Khatibzadeh, S. and Khera, S. and Khoja, T. A. M. and Khubchandani, J. and Kieling, C. and Kim, C.-i. and Kim, D. and Kimokoti, R. W. and Kissoon, N. and Kivipelto, M. and Knibbs, L. D. and Kokubo, Y. and Kopec, J. A. and Koul, P. A. and Koyanagi, A. and Kravchenko, M. and Kromhout, H. and Krueger, H. and Ku, T. and Defo, B. K. and Kuchenbecker, R. S. and Bicer, B. K. and Kuipers, E. J. and Kumar, G. A. and Kwan, G. F. and Lal, D. K. and Lalloo, R. and Lallukka, T. and Lan, Q. and Larsson, A. and Latif, A. A. and Lawrynowicz, A. E. B. and Leasher, J. L. and Leigh, J. and Leung, J. and Levi, M. and Li, X. and Li, Y. and Liang, J. and Liu, S. and Lloyd, B. K. and Logroscino, G. and Lotufo, P. A. and Lunevicius, R. and MacIntyre, M. and Mahdavi, M. and Majdan, M. and Majeed, A. and Malekzadeh, R. and Malta, D. C. and Manamo, W. A. A. and Mapoma, C. C. and Marcenes, W. and Martin, R. V. and Martinez-Raga, J. and Masiye, F. and Matsushita, K. and Matzopoulos, R. and Mayosi, B. M. and McGrath, J. J. and McKee, M. and Meaney, P. A. and Medina, C. and Mehari, A. and Mejia-Rodriguez, F. and Mekonnen, A. B. and Melaku, Y. A. and Memish, Z. A. and Mendoza, W. and Mensink, G. B. M. and Meretoja, A. and Meretoja, T. J. and Mesfin, Y. M. and Mhimbira, F. A. and Millear, A. and Miller, T. R. and Mills, E. J. and Mirarefin, M. and Misganaw, A. and Mock, C. N. and Mohammadi, A. and Mohammed, S. and Mola, G. L. D. and Monasta, L. and Hernandez, J. C. M. and Montico, M. and Morawska, L. and Mori, R. and Mozaffarian, D. and Mueller, U. O. and Mullany, E. and Mumford, J. E. and Murthy, G. V. S. and Nachega, J. B. and Naheed, A. and Nangia, V. and Nassiri, N. and Newton, J. N. and Ng, M. and Nguyen, Q. L. and Nisar, M. I. and Pete, P. M. N. and Norheim, O. F. and Norman, R. E. and Norrving, B. and Nyakarahuka, L. and Obermeyer, C. M. and Ogbo, F. A. and Oh, I.-H. and Oladimeji, O. and Olivares, P. R. and Olsen, H. and Olusanya, B. O. and Olusanya, J. O. and Opio, J. N. and Oren, E. and Orozco, R. and Ortiz, A. and Ota, E. and Pa, M. and Pana, A. and Park, E.-K. and Parry, C. D. and Parsaeian, M. and Patel, T. and Caicedo, A. J. P. and Patil, S. T. and Patten, S. B. and Patton, G. C. and Pearce, N. and Pereira, D. M. and Perico, N. and Pesudovs, K. and Petzold, M. and Phillips, M. R. and Piel, F. B. and Pillay, J. D. and Plass, D. and Polinder, S. and Pond, C. D. and Pope, C. A. and Pope, D. and Popova, S. and Poulton, R. G. and Pourmalek, F. and Prasad, N. M. and Qorbani, M. and Rabiee, R. H. S. and Radfar, A. and

https://doi.org/10.5194/egusphere-2025-1360
Preprint. Discussion started: 5 May 2025

Rafay, A. and Rahimi-Movaghar, V. and Rahman, M. and Rahman, M. H. U. and Rahman, S. U. and Rai, R. K. and Rajsic, S. and Raju, M. and Ram, U. and Rana, S. M. and Ranganathan, K. and Rao, P. and García, C. A. R. and Refaat, A. H. and Rehm, C. D. and Rehm, J. and Reinig, N. and Remuzzi, G. and Resnikoff, S. and Ribeiro, A. L. and Rivera, J. A. and Roba, H. S. and Rodriguez, A. and Rodriguez-Ramirez, S. and Rojas-Rueda, D. and Roman, Y. and Ronfani, L. and Roshandel, G. and Rothenbacher, D. and Roy, A. and Saleh, M. M. and Sanabria, J. R. and Sanchez-Riera, L. and Sanchez-Niño, M. D. and Sánchez-Pimienta, T. G. and Sandar, L. and Santomauro, D. F. and Santos, I. S. and Sarmiento-Suarez, R. and Sartorius, B. and Satpathy, M. and Savic, M. and Sawhney, M. and Schmidhuber, J. and Schmidt, M. I. and Schneider, I. J. C. and Schöttker, B. and Schutte, A. E. and Schwebel, D. C. and Scott, J. G. and Seedat, S. and Sepanlou, S. G. and Servan-Mori, E. E. and Shaddick, G. and Shaheen, A. and Shahraz, S. and Shaikh, M. A. and Levy, T. S. and Sharma, R. and She, J. and Sheikhbahaei, S. and Shen, J. and Sheth, K. N. and Shi, P. and Shibuya, K. and Shigematsu, M. and Shin, M.-J. and Shiri, R. and Shishani, K. and Shiue, I. and Shrime, M. G. and Sigfusdottir, I. D. and Silva, D. A. S. and Silveira, D. G. A. and Silverberg, J. I. and Simard, E. P. and Sindi, S. and Singh, A. and Singh, J. A. and Singh, P. K. and Slepak, E. L. and Soljak, M. and Soneji, S. and Sorensen, R. J. D. and Sposato, L. A. and Sreeramareddy, C. T. and Stathopoulou, V. and Steckling, N. and Steel, N. and Stein, D. J. and Stein, M. B. and Stöckl, H. and Stranges, S. and Stroumpoulis, K. and Sunguya, B. F. and Swaminathan, S. and Sykes, B. L. and Szoeke, C. E. I. and Tabarés-Seisdedos, R. and Takahashi, K. and Talongwa, R. T. and Tandon, N. and Tanne, D. and Tavakkoli, M. and Taye, B. W. and Taylor, H. R. and Tedla, B. A. and Tefera, W. M. and Tegegne, T. K. and Tekle, D. Y. and Terkawi, A. S. and Thakur, J. S. and Thomas, B. A. and Thomas, M. L. and Thomson, A. J. and Thorne-Lyman, A. L. and Thrift, A. G. and Thurston, G. D. and Tillmann, T. and Tobe-Gai, R. and Tobollik, M. and Topor-Madry, R. and Topouzis, F. and Towbin, J. A. and Tran, B. X. and Dimbuene, Z. T. and Tsilimparis, N. and Tura, A. K. and Tuzcu, E. M. and Tyrovolas, S. and Ukwaja, K. N. and Undurraga, E. A. and Uneke, C. J. and Uthman, O. A. and van Donkelaar, A. and van Os, J. and Varakin, Y. Y. and Vasankari, T. and Veerman, J. L. and Venketasubramanian, N. and Violante, F. S. and Vollset, S. E. and Wagner, G. R. and Waller, S. G. and Wang, J. L. and Wang, L. and Wang, Y. and Weichenthal, S. and Weiderpass, E. and Weintraub, R. G. and Werdecker, A. and Westerman, R. and Whiteford, H. A. and Wijeratne, T. and Wiysonge, C. S. and Wolfe, C. D. A. and Won, S. and Woolf, A. D. and Wubshet, M. and Xavier, D. and Xu, G. and Yadav, A. K. and Yakob, B. and Yalew, A. Z. and Yano, Y. and Yaseri, M. and Ye, P. and Yip, P. and Yonemoto, N. and Yoon, S.-J. and Younis, M. Z. and Yu, C. and Zaidi, Z. and Zaki, M. E. S. and Zhu, J. and Zipkin, B. and Zodpey, S. and Zuhlke, L. J. and Murray, C. J. L.: Global, regional, and national comparative risk assessment of 79 behavioural, environmental and occupational, and metabolic risks or clusters of risks, 1990–2015: a systematic analysis for the Global Burden of Disease Study 2015, The Lancet, 388, 1659-1724, https://doi.org/10.1016/S0140-6736(16)31679-8, 2016.

Friedl, M. A., McIver, D. K., Hodges, J. C. F., Zhang, X. Y., Muchoney, D., Strahler, A. H., Woodcock, C. E., Gopal, S., Schneider, A., Cooper, A., Baccini, A., Gao, F., and Schaaf, C.: Global land cover mapping from MODIS: algorithms and early results, Remote Sensing of Environment, 83, 287-302, https://doi.org/10.1016/S0034-4257(02)00078-0, 2002.

Gao, Y., Leung, L. R., Zhao, C., and Hagos, S.: Sensitivity of U.S. summer precipitation to model resolution and convective parameterizations across gray zone resolutions, Journal of Geophysical Research: Atmospheres, 122, 2714-2733, https://doi.org/10.1002/2016JD025896, 2017.

Ge, C., Wang, J., and Reid, J.: Mesoscale modeling of smoke transport over the Southeast Asian Maritime Continent: coupling of smoke direct radiative effect below and above the low-level clouds, Atmospheric Chemistry and Physics, 14, 159-174, 2014.

Ge, C., Wang, J., Reid, J. S., Posselt, D. J., Xian, P., and Hyer, E.: Mesoscale modeling of smoke transport from equatorial Southeast Asian Maritime Continent to the Philippines: First comparison of ensemble analysis with in situ observations, Journal of Geophysical Research: Atmospheres, 122, 5380-5398, 2017.

Gelaro, R., McCarty, W., Suárez, M. J., Todling, R., Molod, A., Takacs, L., Randles, C. A., Darmenov, A., Bosilovich, M. G., and Reichle, R.: The modern-era retrospective analysis for research and applications, version 2 (MERRA-2), Journal of Climate, 30, 5419-5454, 2017.

Georgiou, G. K., Christoudias, T., Proestos, Y., Kushta, J., Hadjinicolaou, P., and Lelieveld, J.: Air quality modelling in the summer over the eastern Mediterranean using WRF-Chem: chemistry and aerosol mechanism intercomparison, Atmospheric Chemistry and Physics, 18, 1555-1571, 2018.

Gettelman, A., Mills, M. J., Kinnison, D. E., Garcia, R. R., Smith, A. K., Marsh, D. R., Tilmes, S., Vitt, F., Bardeen, C. G., McInerny, J., Liu, H.-L., Solomon, S. C., Polvani, L. M., Emmons, L. K., Lamarque, J.-F., Richter, J. H., Glanville, A. S., Bacmeister, J. T., Phillips, A. S., Neale, R. B., Simpson, I. R., DuVivier, A. K., Hodzic, A., and Randel, W. J.: The Whole Atmosphere Community Climate Model Version 6 (WACCM6), Journal of Geophysical Research: Atmospheres, 124, 12380-12403, https://doi.org/10.1029/2019JD030943, 2019.

Gilleland, E., Ahijevych, D., Brown, B. G., Casati, B., and Ebert, E. E.: Intercomparison of spatial forecast verification methods, Weather and forecasting, 24, 1416-1430, 2009.

Ginoux, P., Chin, M., Tegen, I., Prospero, J. M., Holben, B., Dubovik, O., and Lin, S. J.: Sources and distributions of dust aerosols simulated with the GOCART model, Journal of Geophysical Research: Atmospheres, 106, 20255-20273, 2001.

https://doi.org/10.5194/egusphere-2025-1360
Preprint. Discussion started: 5 May 2025

Grell, G. A. and Dévényi, D.: A generalized approach to parameterizing convection combining ensemble and data assimilation techniques, Geophysical Research Letters, 29, 38-31-38-34, 2002.
Grell, G. A. and Freitas, S. R.: A scale and aerosol aware stochastic convective parameterization for weather and air quality modeling, Atmospheric Chemistry and Physics, 14, 5233-5250, 2014.
Grell, G. A., Dudhia, J., and Stauffer, D. R.: A description of the fifth-generation Penn State/NCAR Mesoscale Model (MM5), 1994.
Grell, G. A., Peckham, S. E., Schmitz, R., McKeen, S. A., Frost, G., Skamarock, W. C., and Eder, B.: Fully coupled "online" chemistry within the WRF model, Atmospheric Environment, 39, 6957-6975, 2005.
Guenther, A., Karl, T., Harley, P., Wiedinmyer, C., Palmer, P., and Geron, C.: Estimates of global terrestrial isoprene emissions using MEGAN (Model of Emissions of Gases and Aerosols from Nature), 2006.
Guenther, A., Jiang, X., Heald, C., Sakulyanontvittaya, T., Duhl, T., Emmons, L., and Wang, X.: The Model of Emissions of Gases and Aerosols from Nature version 2.1 (MEGAN2. 1): an extended and updated framework for modeling biogenic emissions, 2012.
Han, B., Fan, J., Varble, A., Morrison, H., Williams, C. R., Chen, B., Dong, X., Giangrande, S. E., Khain, A., Mansell, E., Milbrandt, J. A., Shpund, J., and Thompson, G.: Cloud-Resolving Model Intercomparison of an MC3E Squall Line Case: Part II. Stratiform Precipitation Properties, Journal of Geophysical Research: Atmospheres, 124, 1090-1117, https://doi.org/10.1029/2018JD029596, 2019.
Han, T., Pan, X., and Wang, X.: Evaluating and improving the sand storm numerical simulation performance in Northwestern China using WRF-Chem and remote sensing soil moisture data, Atmospheric Research, 251, 105411, https://doi.org/10.1016/j.atmosres.2020.105411, 2021.
He, X., Li, Y., Wang, X., Chen, L., Yu, B., Zhang, Y., and Miao, S.: High-resolution dataset of urban canopy parameters for Beijing and its application to the integrated WRF/Urban modelling system, Journal of Cleaner Production, 208, 373-383, https://doi.org/10.1016/j.jclepro.2018.10.086, 2019.
Holloway, T., Miller, D., Anenberg, S., Diao, M., Duncan, B., Fiore, A. M., Henze, D. K., Hess, J., Kinney, P. L., Liu, Y., Neu, J. L., O'Neill, S. M., Odman, M. T., Pierce, R. B., Russell, A. G., Tong, D., West, J. J., and Zondlo, M. A.: Satellite Monitoring for Air Quality and Health, Annual Review of Biomedical Data Science, 4, null, 10.1146/annurev-biodatasci-110920-093120, 2021.
Hong, S.-Y. and Lim, J.-O. J.: The WRF single-moment 6-class microphysics scheme (WSM6), Asia-Pacific Journal of Atmospheric Sciences, 42, 129-151, 2006.
Hong, S.-Y., Noh, Y., and Dudhia, J.: A new vertical diffusion package with an explicit treatment of entrainment processes, Monthly weather review, 134, 2318-2341, 2006.
Hu, J., Ostro, B., Zhang, H., Ying, Q., and Kleeman, M. J.: Using Chemical Transport Model Predictions To Improve Exposure Assessment of PM2.5 Constituents, Environmental Science & Technology Letters, 6, 456-461, 10.1021/acs.estlett.9b00396, 2019.
Hudman, R., Moore, N., Mebust, A., Martin, R., Russell, A., Valin, L., and Cohen, R.: Steps towards a mechanistic model of global soil nitric oxide emissions: implementation and space based-constraints, Atmospheric Chemistry & Physics, 12, 2012.
Hyde, P., Mahalov, A., and Li, J.: Simulating the meteorology and PM10 concentrations in Arizona dust storms using the Weather Research and Forecasting model with Chemistry (Wrf-Chem), Journal of the Air & Waste Management Association, 68, 177-195, 2018.
Iacono, M. J., Delamere, J. S., Mlawer, E. J., Shephard, M. W., Clough, S. A., and Collins, W. D.: Radiative forcing by long-lived greenhouse gases: Calculations with the AER radiative transfer models, Journal of Geophysical Research: Atmospheres, 113, 2008.
Ichoku, C. and Ellison, L.: Global top-down smoke-aerosol emissions estimation using satellite fire radiative power measurements, Atmospheric Chemistry and Physics, 14, 6643-6667, 2014.
Jaeglé, L., Steinberger, L., Martin, R. V., and Chance, K.: Global partitioning of NO x sources using satellite observations: Relative roles of fossil fuel combustion, biomass burning and soil emissions, Faraday discussions, 130, 407-423, 2005.
Janjic, Z.: Nonsingular implementation of the Mellor-Yamada Level 2.5 Scheme in the NCEP Meso model, National Centers for Environmental Prediction, Office Note, 2001.
Janssens-Maenhout, G., Crippa, M., Guizzardi, D., Dentener, F., Muntean, M., Pouliot, G., Keating, T., Zhang, Q., Kurokawa, J., Wankmüller, R., Denier van der Gon, H., Kuenen, J. J. P., Klimont, Z., Frost, G., Darras, S., Koffi, B., and Li, M.: HTAP_v2.2: a mosaic of regional and global emission grid maps for 2008 and 2010 to study hemispheric transport of air pollution, Atmos. Chem. Phys., 15, 11411-11432, 10.5194/acp-15-11411-2015, 2015.
Jenkins, G. S. and Diokhane, A. M.: WRF prediction of two winter season Saharan dust events using PM10 concentrations: Boundary versus initial conditions, Atmospheric Environment, 167, 129-142, https://doi.org/10.1016/j.atmosenv.2017.08.010, 2017.
Jeworrek, J., West, G., and Stull, R.: Evaluation of cumulus and microphysics parameterizations in WRF across the convective gray zone, Weather and Forecasting, 34, 1097-1115, 2019.

https://doi.org/10.5194/egusphere-2025-1360
Preprint. Discussion started: 5 May 2025

Jeworrek, J., West, G., and Stull, R.: WRF precipitation performance and predictability for systematically varied parameterizations over complex terrain, Weather and Forecasting, 36, 893-913, 2021.
Jiménez, P. A. and Dudhia, J.: Improving the representation of resolved and unresolved topographic effects on surface wind in the WRF model, Journal of Applied Meteorology and Climatology, 51, 300-316, 2012.
Jiménez, P. A., Dudhia, J., González-Rouco, J. F., Navarro, J., Montávez, J. P., and García-Bustamante, E.: A Revised Scheme for the WRF Surface Layer Formulation, Monthly Weather Review, 140, 898-918, https://doi.org/10.1175/MWR-D-11-00056.1, 2012.
Jung, E. and Shao, Y.: An intercomparison of four wet deposition schemes used in dust transport modeling, Global and Planetary Change, 52, 248-260, https://doi.org/10.1016/j.gloplacha.2006.02.008, 2006.
Justice, C., Townshend, J., Vermote, E., Masuoka, E., Wolfe, R., Saleous, N., Roy, D., and Morisette, J.: An overview of MODIS Land data processing and product status, Remote sensing of Environment, 83, 3-15, 2002.
Kahn, R. A., Gaitley, B. J., Martonchik, J. V., Diner, D. J., Crean, K. A., and Holben, B.: Multiangle Imaging Spectroradiometer (MISR) global aerosol optical depth validation based on 2 years of coincident Aerosol Robotic Network (AERONET) observations, Journal of Geophysical Research: Atmospheres, 110, 2005.
Kaiser, J., Heil, A., Andreae, M., Benedetti, A., Chubarova, N., Jones, L., Morcrette, J.-J., Razinger, M., Schultz, M., and Suttie, M.: Biomass burning emissions estimated with a global fire assimilation system based on observed fire radiative power, Biogeosciences, 9, 527-554, 2012.
Kim, J., Jeong, U., Ahn, M.-H., Kim, J. H., Park, R. J., Lee, H., Song, C. H., Choi, Y.-S., Lee, K.-H., and Yoo, J.-M.: New era of air quality monitoring from space: Geostationary Environment Monitoring Spectrometer (GEMS), Bulletin of the American Meteorological Society, 101, E1-E22, 2020.
Klein, C., Heinzeller, D., Bliefernicht, J., and Kunstmann, H.: Variability of West African monsoon patterns generated by a WRF multi-physics ensemble, Climate Dynamics, 45, 2733-2755, 2015.
Koster, R. D., Suarez, M. J., Ducharne, A., Stieglitz, M., and Kumar, P.: A catchment-based approach to modeling land surface processes in a general circulation model: 1. Model structure, Journal of Geophysical Research: Atmospheres, 105, 24809-24822, 2000.
Kumar, S. V., Peters-Lidard, C. D., Eastman, J. L., and Tao, W.-K.: An integrated high-resolution hydrometeorological modeling testbed using LIS and WRF, Environmental Modelling & Software, 23, 169-181, 2008.
Kumar, S. V., Peters-Lidard, C. D., Tian, Y., Houser, P. R., Geiger, J., Olden, S., Lighty, L., Eastman, J. L., Doty, B., Dirmeyer, P., Adams, J., Mitchell, K., Wood, E. F., and Sheffield, J.: Land information system: An interoperable framework for high resolution land surface modeling, Environmental Modelling & Software, 21, 1402-1415, https://doi.org/10.1016/j.envsoft.2005.07.004, 2006.
Lee, J., Hsu, N. C., Sayer, A. M., Bettenhausen, C., and Yang, P.: AERONET-Based Nonspherical Dust Optical Models and Effects on the VIIRS Deep Blue/SOAR Over Water Aerosol Product, Journal of Geophysical Research: Atmospheres, 122, 10,384-310,401, https://doi.org/10.1002/2017JD027258, 2017.
LeGrand, S. L., Polashenski, C., Letcher, T. W., Creighton, G. A., Peckham, S. E., and Cetola, J. D.: The AFWA dust emission scheme for the GOCART aerosol model in WRF-Chem v3. 8.1, Geoscientific Model Development, 12, 131, 2019.
LeGrand, S. L., Letcher, T. W., Okin, G. S., Webb, N. P., Gallagher, A. R., Dhital, S., Hodgdon, T. S., Ziegler, N. P., and Michaels, M. L.: Application of a satellite-retrieved sheltering parameterization (v1. 0) for dust event simulation with WRF-Chem v4. 1, Geoscientific Model Development, 16, 1009-1038, 2023.
Li, C., Wang, J., Zhang, H., Diner, D. J., Hasheminassab, S., and Janechek, N.: Improvement of Surface PM2. 5 Diurnal Variation Simulations in East Africa for the MAIA Satellite Mission, ACS ES&T Air, 2024.
Li, M., Song, Y., Huang, X., Li, J., Mao, Y., Zhu, T., Cai, X., and Liu, B.: Improving mesoscale modeling using satellite-derived land surface parameters in the Pearl River Delta region, China, Journal of Geophysical Research: Atmospheres, 119, 6325-6346, 2014.
Li, M., Wang, T., Xie, M., Zhuang, B., Li, S., Han, Y., Song, Y., and Cheng, N.: Improved meteorology and ozone air quality simulations using MODIS land surface parameters in the Yangtze River Delta urban cluster, China, Journal of Geophysical Research: Atmospheres, 122, 3116-3140, 2017a.
Li, M., Liu, H., Geng, G., Hong, C., Liu, F., Song, Y., Tong, D., Zheng, B., Cui, H., and Man, H.: Anthropogenic emission inventories in China: a review, National Science Review, 4, 834-866, 2017b.
Li, Y., Pickering, K. E., Barth, M. C., Bela, M. M., Cummings, K. A., and Allen, D. J.: Evaluation of Parameterized Convective Transport of Trace Gases in Simulation of Storms Observed During the DC3 Field Campaign, Journal of Geophysical Research: Atmospheres, 123, 11,238-211,261, https://doi.org/10.1029/2018JD028779, 2018.
Li, Y., Pickering, K. E., Barth, M. C., Bela, M. M., Cummings, K. A., and Allen, D. J.: Wet Scavenging in WRF-Chem Simulations of Parameterized Convection for a Severe Storm During the DC3 Field Campaign, Journal of Geophysical Research: Atmospheres, 124, 7413-7428, https://doi.org/10.1029/2019JD030484, 2019.

https://doi.org/10.5194/egusphere-2025-1360
Preprint. Discussion started: 5 May 2025

Li, Y., Yuan, S., Fan, S., Song, Y., Wang, Z., Yu, Z., Yu, Q., and Liu, Y.: Satellite Remote Sensing for Estimating PM 2.5 and Its Components, Current Pollution Reports, 1-16, 2021.

Liang, T., He, J., Chen, L., Yao, Z., Zhang, L., Che, H., and Gong, S.: Simulation of the influence of a fine-scale urban underlying surface on the urban heat island effect in Beijing, Atmospheric Research, 262, 105786, https://doi.org/10.1016/j.atmosres.2021.105786, 2021.

Lin, Y.-C., Zhang, Y.-L., Yu, M., Fan, M.-Y., Xie, F., Zhang, W.-Q., Wu, G., Cong, Z., and Michalski, G.: Formation Mechanisms and Source Apportionments of Airborne Nitrate Aerosols at a Himalayan-Tibetan Plateau Site: Insights from Nitrogen and Oxygen Isotopic Compositions, Environmental Science & Technology, 55, 12261-12271, 2021.

Lin, Y.-L., Farley, R. D., and Orville, H. D.: Bulk parameterization of the snow field in a cloud model, Journal of Applied Meteorology and climatology, 22, 1065-1092, 1983.

Liu, Y. and Diner, D. J.: Multi-angle imager for aerosols: a satellite investigation to benefit public health, Public Health Reports, 132, 14-17, 2017.

Liu, Y., Chen, D., Kahn, R. A., and He, K.: Review of the applications of multiangle imaging spectroradiometer to air quality research, Science in China Series D: Earth Sciences, 52, 132-144, 2009.

Meng, X., Garay, M. J., Diner, D. J., Kalashnikova, O. V., Xu, J., and Liu, Y.: Estimating PM2. 5 speciation concentrations using prototype 4.4 km-resolution MISR aerosol properties over Southern California, Atmospheric Environment, 181, 70-81, 2018.

Mitchell, K. E., Lohmann, D., Houser, P. R., Wood, E. F., Schaake, J. C., Robock, A., Cosgrove, B. A., Sheffield, J., Duan, Q., and Luo, L.: The multi-institution North American Land Data Assimilation System (NLDAS): Utilizing multiple GCIP products and partners in a continental distributed hydrological modeling system, Journal of Geophysical Research: Atmospheres, 109, 2004.

Mlawer, E. J., Taubman, S. J., Brown, P. D., Iacono, M. J., and Clough, S. A.: Radiative transfer for inhomogeneous atmospheres: RRTM, a validated correlated-k model for the longwave, Journal of Geophysical Research: Atmospheres, 102, 16663-16682, 1997.

Mo, J., Gong, S., Zhang, L., He, J., Lu, S., Zhou, Y., Ke, H., and Zhang, H.: Impacts of long-range transports from Central and South Asia on winter surface PM2. 5 concentrations in China, Science of The Total Environment, 777, 146243, 2021.

Mölders, N.: On the uncertainty in mesoscale modeling caused by surface parameters, Meteorology and Atmospheric Physics, 76, 119-141, 2001.

Morrison, H., Thompson, G., and Tatarskii, V.: Impact of cloud microphysics on the development of trailing stratiform precipitation in a simulated squall line: Comparison of one-and two-moment schemes, Monthly weather review, 137, 991-1007, 2009.

Nakanishi, M. and Niino, H.: An Improved Mellor–Yamada Level-3 Model with Condensation Physics: Its Design and Verification, Boundary-Layer Meteorology, 112, 1-31, 10.1023/B:BOUN.0000020164.04146.98, 2004.

Oikawa, P. Y., Ge, C., Wang, J., Eberwein, J. R., Liang, L. L., Allsman, L. A., Grantz, D. A., and Jenerette, G. D.: Unusually high soil nitrogen oxide emissions influence air quality in a high-temperature agricultural region, Nature Communications, 6, 8753, 10.1038/ncomms9753, 2015.

Oleson, K. W., Dai, Y., Bonan, G., Bosilovich, M., Dickinson, R., Dirmeyer, P., Hoffman, F., Houser, P., Levis, S., and Niu, G.-Y.: Technical description of the community land model (CLM), Tech. Note NCAR/TN-461+ STR, 2004.

Peters-Lidard, C. D., Kemp, E. M., Matsui, T., Santanello, J. A., Kumar, S. V., Jacob, J. P., Clune, T., Tao, W.-K., Chin, M., Hou, A., Case, J. L., Kim, D., Kim, K.-M., Lau, W., Liu, Y., Shi, J., Starr, D., Tan, Q., Tao, Z., Zaitchik, B. F., Zavodsky, B., Zhang, S. Q., and Zupanski, M.: Integrated modeling of aerosol, cloud, precipitation and land processes at satellite-resolved scales, Environmental Modelling & Software, 67, 149-159, https://doi.org/10.1016/j.envsoft.2015.01.007, 2015.

Pey, J., Querol, X., Alastuey, A., Forastiere, F., and Stafoggia, M.: African dust outbreaks over the Mediterranean Basin during 2001–2011: PM₁₀ concentrations, phenomenology and trends, and its relation with synoptic and mesoscale meteorology, Atmos. Chem. Phys., 13, 1395-1410, 10.5194/acp-13-1395-2013, 2013.

Philip, S., Martin, R. V., van Donkelaar, A., Lo, J. W.-H., Wang, Y., Chen, D., Zhang, L., Kasibhatla, P. S., Wang, S., and Zhang, Q.: Global chemical composition of ambient fine particulate matter for exposure assessment, Environmental science & technology, 48, 13060-13068, 2014.

Prein, A. F., Langhans, W., Fosser, G., Ferrone, A., Ban, N., Goergen, K., Keller, M., Tölle, M., Gutjahr, O., Feser, F., Brisson, E., Kollet, S., Schmidli, J., van Lipzig, N. P. M., and Leung, R.: A review on regional convection-permitting climate modeling: Demonstrations, prospects, and challenges, Reviews of Geophysics, 53, 323-361, https://doi.org/10.1002/2014RG000475, 2015.

Querol, X., Pey, J., Pandolfi, M., Alastuey, A., Cusack, M., Pérez, N., Moreno, T., Viana, M., Mihalopoulos, N., Kallos, G., and Kleanthous, S.: African dust contributions to mean ambient PM10 mass-levels across the Mediterranean Basin, Atmospheric Environment, 43, 4266-4277, https://doi.org/10.1016/j.atmosenv.2009.06.013, 2009.

Randles, C., Da Silva, A., Buchard, V., Colarco, P., Darmenov, A., Govindaraju, R., Smirnov, A., Holben, B., Ferrare, R., and Hair, J.: The MERRA-2 aerosol reanalysis, 1980 onward. Part I: System description and data assimilation evaluation, Journal of Climate, 30, 6823-6850, 2017.

https://doi.org/10.5194/egusphere-2025-1360
Preprint. Discussion started: 5 May 2025

Reid, J. S., Hyer, E. J., Prins, E. M., Westphal, D. L., Zhang, J., Wang, J., Christopher, S. A., Curtis, C. A., Schmidt, C. C., and Eleuterio, D. P.: Global monitoring and forecasting of biomass-burning smoke: Description of and lessons from the Fire Locating and Modeling of Burning Emissions (FLAMBE) program, IEEE Journal of Selected Topics in Applied Earth Observations and Remote Sensing, 2, 144-162, 2009.

Rienecker, M. M., Suarez, M., Todling, R., Bacmeister, J., Takacs, L., Liu, H., Gu, W., Sienkiewicz, M., Koster, R., and Gelaro, R.: The GEOS-5 Data Assimilation System: Documentation of Versions 5.0. 1, 5.1. 0, and 5.2. 0, 2008.

Roberts, G. J. and Wooster, M. J.: Fire detection and fire characterization over Africa using Meteosat SEVIRI, IEEE Transactions on Geoscience and Remote Sensing, 46, 1200-1218, 2008.

Rodell, M., Houser, P., Jambor, U., Gottschalck, J., Mitchell, K., Meng, C.-J., Arsenault, K., Cosgrove, B., Radakovich, J., and Bosilovich, M.: The global land data assimilation system, Bulletin of the American Meteorological Society, 85, 381-394, 2004.

Roozitalab, B., Carmichael, G. R., and Guttikunda, S. K.: Improving regional air quality predictions in the Indo-Gangetic Plain–case study of an intensive pollution episode in November 2017, Atmospheric Chemistry and Physics, 21, 2837-2860, 2021.

Rossa, A., Nurmi, P., and Ebert, E.: Overview of methods for the verification of quantitative precipitation forecasts, in: Precipitation: Advances in measurement, estimation and prediction, Springer, 419-452, 2008.

Schell, B., Ackermann, I. J., Hass, H., Binkowski, F. S., and Ebel, A.: Modeling the formation of secondary organic aerosol within a comprehensive air quality model system, Journal of Geophysical Research: Atmospheres, 106, 28275-28293, 2001.

Sha, T., Ma, X., Zhang, H., Janechek, N., Wang, Y., Wang, Y., Castro García, L., Jenerette, G. D., and Wang, J.: Impacts of Soil NOx Emission on O3 Air Quality in Rural California, Environmental Science & Technology, 10.1021/acs.est.0c06834, 2021.

Shao, Y., Ishizuka, M., Mikami, M., and Leys, J.: Parameterization of size-resolved dust emission and validation with measurements, Journal of Geophysical Research: Atmospheres, 116, 2011.

Shin, M., Kang, Y., Park, S., Im, J., Yoo, C., and Quackenbush, L. J.: Estimating ground-level particulate matter concentrations using satellite-based data: a review, GIScience & Remote Sensing, 57, 174-189, 2020.

Silvern, R. F., Jacob, D. J., Mickley, L. J., Sulprizio, M. P., Travis, K. R., Marais, E. A., Cohen, R. C., Laughner, J. L., Choi, S., Joiner, J., and Lamsal, L. N.: Using satellite observations of tropospheric NO2 columns to infer long-term trends in US NOx emissions: the importance of accounting for the free tropospheric NO2 background, Atmos. Chem. Phys., 19, 8863-8878, 10.5194/acp-19-8863-2019, 2019.

Smirnova, T. G., Brown, J. M., Benjamin, S. G., and Kim, D.: Parameterization of cold-season processes in the MAPS land-surface scheme, Journal of Geophysical Research: Atmospheres, 105, 4077-4086, https://doi.org/10.1029/1999JD901047, 2000.

Snider, G., Weagle, C. L., Martin, R. V., van Donkelaar, A., Conrad, K., Cunningham, D., Gordon, C., Zwicker, M., Akoshile, C., Artaxo, P., Anh, N. X., Brook, J., Dong, J., Garland, R. M., Greenwald, R., Griffith, D., He, K., Holben, B. N., Kahn, R., Koren, I., Lagrosas, N., Lestari, P., Ma, Z., Vanderlei Martins, J., Quel, E. J., Rudich, Y., Salam, A., Tripathi, S. N., Yu, C., Zhang, Q., Zhang, Y., Brauer, M., Cohen, A., Gibson, M. D., and Liu, Y.: SPARTAN: a global network to evaluate and enhance satellite-based estimates of ground-level particulate matter for global health applications, Atmos. Meas. Tech., 8, 505-521, 10.5194/amt-8-505-2015, 2015.

Stockwell, W. R., Middleton, P., Chang, J. S., and Tang, X.: The second generation regional acid deposition model chemical mechanism for regional air quality modeling, Journal of Geophysical Research: Atmospheres, 95, 16343-16367, 1990.

Su, L. and Fung, J. C. H.: Sensitivities of WRF-Chem to dust emission schemes and land surface properties in simulating dust cycles during springtime over East Asia, Journal of Geophysical Research: Atmospheres, 120, 11,215-211,230, https://doi.org/10.1002/2015JD023446, 2015.

Taylor, K. E.: Summarizing multiple aspects of model performance in a single diagram, Journal of Geophysical Research: Atmospheres, 106, 7183-7192, 2001.

Thomas, A., Huff, A. K., Hu, X.-M., and Zhang, F.: Quantifying Uncertainties of Ground-Level Ozone Within WRF-Chem Simulations in the Mid-Atlantic Region of the United States as a Response to Variability, Journal of Advances in Modeling Earth Systems, 11, 1100-1116, https://doi.org/10.1029/2018MS001457, 2019.

Tsarpalis, K., Papadopoulos, A., Mihalopoulos, N., Spyrou, C., Michaelides, S., and Katsafados, P.: The implementation of a mineral dust wet deposition scheme in the GOCART-AFWA module of the WRF model, Remote Sensing, 10, 1595, 2018.

Tuccella, P., Curci, G., Visconti, G., Bessagnet, B., Menut, L., and Park, R. J.: Modeling of gas and aerosol with WRF/Chem over Europe: Evaluation and sensitivity study, Journal of Geophysical Research: Atmospheres, 117, 2012.

Ukhov, A., Ahmadov, R., Grell, G., and Stenchikov, G.: Improving dust simulations in WRF-Chem v4.1.3 coupled with the GOCART aerosol module, Geosci. Model Dev., 14, 473-493, 10.5194/gmd-14-473-2021, 2021.

Ukhov, A., Mostamandi, S., Krotkov, N., Flemming, J., da Silva, A., Li, C., Fioletov, V., McLinden, C., Anisimov, A., and Alshehri, Y. M.: Study of SO Pollution in the Middle East Using MERRA-2, CAMS Data Assimilation Products, and High-Resolution WRF-Chem Simulations, Journal of Geophysical Research: Atmospheres, 125, e2019JD031993, 2020.

https://doi.org/10.5194/egusphere-2025-1360
Preprint. Discussion started: 5 May 2025

Van der Werf, G. R., Randerson, J. T., Giglio, L., Collatz, G., Mu, M., Kasibhatla, P. S., Morton, D. C., DeFries, R., Jin, Y. v., and van Leeuwen, T. T.: Global fire emissions and the contribution of deforestation, savanna, forest, agricultural, and peat fires (1997–2009), Atmospheric chemistry and physics, 10, 11707-11735, 2010.

Van Donkelaar, A., Martin, R. V., and Park, R. J.: Estimating ground-level PM2. 5 using aerosol optical depth determined from satellite remote sensing, Journal of Geophysical Research: Atmospheres, 111, 2006.

Van Donkelaar, A., Martin, R. V., Brauer, M., Kahn, R., Levy, R., Verduzco, C., and Villeneuve, P. J.: Global estimates of ambient fine particulate matter concentrations from satellite-based aerosol optical depth: development and application, Environmental health perspectives, 118, 847, 2010.

Viana, M., Pey, J., Querol, X., Alastuey, A., de Leeuw, F., and Lükewille, A.: Natural sources of atmospheric aerosols influencing air quality across Europe, Science of The Total Environment, 472, 825-833, https://doi.org/10.1016/j.scitotenv.2013.11.140, 2014.

Vinken, G., Boersma, K., Maasakkers, J., Adon, M., and Martin, R.: Worldwide biogenic soil NO x emissions inferred from OMI NO 2 observations, Atmospheric Chemistry and Physics, 14, 10363-10381, 2014.

Wagner, A., Heinzeller, D., Wagner, S., Rummler, T., and Kunstmann, H.: Explicit convection and scale-aware cumulus parameterizations: High-resolution simulations over areas of different topography in Germany, Monthly Weather Review, 146, 1925-1944, 2018.

Wang, J. and Christopher, S. A.: Intercomparison between satellite-derived aerosol optical thickness and PM2. 5 mass: Implications for air quality studies, Geophysical research letters, 30, 2003.

Wang, J., Nair, U., and Christopher, S. A.: GOES 8 aerosol optical thickness assimilation in a mesoscale model: Online integration of aerosol radiative effects, Journal of Geophysical Research: Atmospheres, 109, 2004.

Wang, J., Huang, B., Fu, D., Atkinson, P. M., and Zhang, X.: Response of urban heat island to future urban expansion over the Beijing–Tianjin–Hebei metropolitan area, Applied Geography, 70, 26-36, 2016.

Wang, J., Ge, C., Yang, Z., Hyer, E. J., Reid, J. S., Chew, B.-N., Mahmud, M., Zhang, Y., and Zhang, M.: Mesoscale modeling of smoke transport over the Southeast Asian Maritime Continent: Interplay of sea breeze, trade wind, typhoon, and topography, Atmospheric Research, 122, 486-503, 2013.

Wang, L., Wu, X., Du, J., Cao, W., and Sun, S.: Global burden of ischemic heart disease attributable to ambient PM2.5 pollution from 1990 to 2017, Chemosphere, 263, 128134, https://doi.org/10.1016/j.chemosphere.2020.128134, 2021a.

Wang, Q., Gu, J., and Wang, X.: The impact of Sahara dust on air quality and public health in European countries, Atmospheric Environment, 241, 117771, https://doi.org/10.1016/j.atmosenv.2020.117771, 2020a.

Wang, R., Qiao, F., Liang, X.-Z., Zhu, Y., Zhang, H., Li, Q., and Ding, Y.: Role of convection representation across the gray zone in forecasting warm season extreme precipitation over Shanghai from two typical cases, Atmospheric Research, 253, 105370, https://doi.org/10.1016/j.atmosres.2020.105370, 2021b.

Wang, Y., Ge, C., Garcia, L. C., Jenerette, G. D., Oikawa, P. Y., and Wang, J.: Improved modelling of soil NO x emissions in a high temperature agricultural region: role of background emissions on NO2 trend over the US, Environmental research letters, 16, 084061, 2021c.

Wang, Y., Wang, J., Xu, X., Henze, D. K., Qu, Z., and Yang, K.: Inverse modeling of SO 2 and NO x emissions over China using multisensor satellite data–Part 1: Formulation and sensitivity analysis, Atmospheric Chemistry and Physics, 20, 6631-6650, 2020b.

Wang, Y., Wang, J., Zhou, M., Henze, D. K., Ge, C., and Wang, W.: Inverse modeling of SO 2 and NO x emissions over China using multisensor satellite data–Part 2: Downscaling techniques for air quality analysis and forecasts, Atmospheric Chemistry and Physics, 20, 6651-6670, 2020c.

Wang, Y., Wang, J., Zhang, H., Janechek, N., Wang, Y., Zhou, M., Shen, P., Tan, J., He, Q., Cheng, T., and Huang, C.: Impact of land use change on the urban-rural temperature disparity in Eastern China, Atmospheric Environment, 308, 119850, https://doi.org/10.1016/j.atmosenv.2023.119850, 2023.

Wei, J., Wang, J., Li, Z., Kondragunta, S., Anenberg, S., Wang, Y., Zhang, H., Diner, D., Hand, J., and Lyapustin, A.: Long-term mortality burden trends attributed to black carbon and PM2· 5 from wildfire emissions across the continental USA from 2000 to 2020: a deep learning modelling study, The Lancet Planetary Health, 7, e963-e975, 2023.

Weisman, M. L., Skamarock, W. C., and Klemp, J. B.: The resolution dependence of explicitly modeled convective systems, Monthly Weather Review, 125, 527-548, 1997.

Weisman, M. L., Davis, C., Wang, W., Manning, K. W., and Klemp, J. B.: Experiences with 0–36-h explicit convective forecasts with the WRF-ARW model, Weather and Forecasting, 23, 407-437, 2008.

Wiedinmyer, C., Akagi, S., Yokelson, R. J., Emmons, L., Al-Saadi, J., Orlando, J., and Soja, A.: The Fire INventory from NCAR (FINN): A high resolution global model to estimate the emissions from open burning, Geoscientific Model Development, 4, 625, 2011.

https://doi.org/10.5194/egusphere-2025-1360
Preprint. Discussion started: 5 May 2025

Wu, J., Bei, N., Wang, Y., Li, X., Liu, S., Liu, L., Wang, R., Yu, J., Le, T., and Zuo, M.: Insights into particulate matter pollution in the North China Plain during wintertime: local contribution or regional transport?, Atmospheric Chemistry and Physics, 21, 2229-2249, 2021.

Xia, Y., Sheffield, J., Ek, M. B., Dong, J., Chaney, N., Wei, H., Meng, J., and Wood, E. F.: Evaluation of multi-model simulated soil moisture in NLDAS-2, Journal of Hydrology, 512, 107-125, https://doi.org/10.1016/j.jhydrol.2014.02.027, 2014.

Yang, Z., Wang, J., Ichoku, C., Hyer, E., and Zeng, J.: Mesoscale modeling and satellite observation of transport and mixing of smoke and dust particles over northern sub-Saharan African region, Journal of Geophysical Research: Atmospheres, 118, 12,139-112,157, 2013.

Yu, E., Bai, R., Chen, X., and Shao, L.: Impact of physical parameterizations on wind simulation with WRF V3.9.1.1 under stable conditions at planetary boundary layer gray-zone resolution: a case study over the coastal regions of North China, Geosci. Model Dev., 15, 8111-8134, 10.5194/gmd-15-8111-2022, 2022.

Zeng, Y., Wang, M., Zhao, C., Chen, S., Liu, Z., Huang, X., and Gao, Y.: WRF-Chem v3. 9 simulations of the East Asian dust storm in May 2017: modeling sensitivities to dust emission and dry deposition schemes, Geoscientific Model Development, 13, 2125-2147, 2020.

Zhang, F., Wang, J., Ichoku, C., Hyer, E. J., Yang, Z., Ge, C., Su, S., Zhang, X., Kondragunta, S., and Kaiser, J. W.: Sensitivity of mesoscale modeling of smoke direct radiative effect to the emission inventory: a case study in northern sub-Saharan African region, Environmental Research Letters, 9, 075002, 2014.

Zhang, G. J. and McFarlane, N. A.: Sensitivity of climate simulations to the parameterization of cumulus convection in the Canadian Climate Centre general circulation model, Atmosphere-ocean, 33, 407-446, 1995.

Zhang, H.: Development of UI-WRF-Chem (v1.0) for the MAIA satellite mission: case demonstration, https://zenodo.org/records/15074108, 2025a.

Zhang, H.: Development of UI-WRF-Chem (v1.0) for the MAIA satellite mission: case demonstration, https://zenodo.org/records/15239059, 2025b.

Zhang, H., Wang, S., Hao, J., Wang, X., Wang, S., Chai, F., and Li, M.: Air pollution and control action in Beijing, Journal of Cleaner Production, 112, 1519-1527, 2016.

Zhang, H., Wang, J., García, L. C., Ge, C., Plessel, T., Szykman, J., Murphy, B., and Spero, T. L.: Improving Surface PM2.5 Forecasts in the United States Using an Ensemble of Chemical Transport Model Outputs: 1. Bias Correction With Surface Observations in Nonrural Areas, Journal of Geophysical Research: Atmospheres, 125, e2019JD032293, 10.1029/2019jd032293, 2020.

Zhang, H., Wang, J., García, L. C., Zhou, M., Ge, C., Plessel, T., Szykman, J., Levy, R. C., Murphy, B., and Spero, T. L.: Improving Surface PM2.5 Forecasts in the United States Using an Ensemble of Chemical Transport Model Outputs: 2. Bias Correction With Satellite Data for Rural Areas, Journal of Geophysical Research: Atmospheres, 127, e2021JD035563, https://doi.org/10.1029/2021JD035563, 2022.

Zhang, X., Kondragunta, S., Ram, J., Schmidt, C., and Huang, H. C.: Near-real-time global biomass burning emissions product from geostationary satellite constellation, Journal of Geophysical Research: Atmospheres, 117, 2012.

Zhang, X.-X., Sharratt, B., Liu, L.-Y., Wang, Z.-F., Pan, X.-L., Lei, J.-Q., Wu, S.-X., Huang, S.-Y., Guo, Y.-H., and Li, J.: East Asian dust storm in May 2017: observations, modelling, and its influence on the Asia-Pacific region, Atmospheric Chemistry and Physics, 18, 8353-8371, 2018.

Zhang, Y., Roundy, J. K., and Santanello, J. A.: Evaluating the impact of model resolutions and cumulus parameterization on precipitation in NU-WRF: A case study in the Central Great Plains, Environmental Modelling & Software, 145, 105184, https://doi.org/10.1016/j.envsoft.2021.105184, 2021.

Zhao, T., Gong, S., Zhang, X., and McKendry, I.: Modeled size-segregated wet and dry deposition budgets of soil dust aerosol during ACE-Asia 2001: Implications for trans-Pacific transport, Journal of Geophysical Research: Atmospheres, 108, 2003.

Zheng, B., Tong, D., Li, M., Liu, F., Hong, C., Geng, G., Li, H., Li, X., Peng, L., Qi, J., Yan, L., Zhang, Y., Zhao, H., Zheng, Y., He, K., and Zhang, Q.: Trends in China's anthropogenic emissions since 2010 as the consequence of clean air actions, Atmos. Chem. Phys., 18, 14095-14111, 10.5194/acp-18-14095-2018, 2018.

Zhou, M., Wang, J., Garcia, L. C., Chen, X., da Silva, A. M., Wang, Z., Román, M. O., Hyer, E. J., and Miller, S. D.: Enhancement of Nighttime Fire Detection and Combustion Efficiency Characterization Using Suomi-NPP and NOAA-20 VIIRS Instruments, IEEE transactions on geoscience and remote sensing, 61, 1-20, 2023.

Zhu, Q., Place, B., Pfannerstill, E. Y., Tong, S., Zhang, H., Wang, J., Nussbaumer, C. M., Wooldridge, P., Schulze, B. C., and Arata, C.: Direct observations of NO x emissions over the San Joaquin Valley using airborne flux measurements during RECAP-CA 2021 field campaign, Atmospheric chemistry and physics, 23, 9669-9683, 2023.

https://doi.org/10.5194/egusphere-2025-1360
Preprint. Discussion started: 5 May 2025

1785 Zoogman, P., Liu, X., Suleiman, R., Pennington, W., Flittner, D., Al-Saadi, J., Hilton, B., Nicks, D., Newchurch, M., and Carr, J.: Tropospheric emissions: Monitoring of pollution (TEMPO), Journal of Quantitative Spectroscopy and Radiative Transfer, 186, 17-39, 2017.